Available online at www.sciencedirect.com

jmr&t Journal of Materials Research and Technology

journal homepage: www.elsevier.com/locate/jmrt

Original Article

Assessment of optical and fluorescence aspects of Er^{3+}-doped multicomponent B_2O_3 glasses as active media for 1.532 μm near-infrared optical amplifiers

G. Lakshminarayana [a,*], A.N. Meza-Rocha [b], O. Soriano-Romero [c], U. Caldiño [d], A. Lira [e], Dong-Eun Lee [f,**], Jonghun Yoon [g,***], Taejoon Park [h,****]

[a] Intelligent Construction Automation Center, Kyungpook National University, 80, Daehak-ro, Buk-gu, Daegu, 41566, Republic of Korea

[b] CONACYT-Benemérita Universidad Autónoma de Puebla, Postgrado en Física Aplicada, Facultad de Ciencias Físico-Matemáticas, Av. San Claudio y Av. 18 sur, Col. San Manuel Ciudad Universitaria, Puebla, Pue 72570, Mexico

[c] Posgrado en Física Aplicada, Facultad de Ciencias Físico-Matemáticas, Benemérita Universidad Autónoma de Puebla, Av. San Claudio y Av. 18 Sur, Col. San Manuel Ciudad Universitaria, Puebla, Pue 72570, Mexico

[d] Departamento de Física, Universidad Autónoma Metropolitana-Iztapalapa, P.O. Box 55-534, México, D.F 09340, Mexico

[e] Departamento de Física, Facultad de Ciencias, Universidad Autónoma del Estado de México, C.P 50000, Toluca, Mexico

[f] School of Architecture, Civil, Environment and Energy, Kyungpook National University, 1370, Sangyeok-dong, Buk-gu, DaeGu, 702-701, Republic of Korea

[g] Department of Mechanical Engineering, BK21 FOUR ERICA-ACE Center, Hanyang University, 55, Hanyangdaehak-ro, Sangnok-gu, Ansan-si, Gyeonggi-do 15588, Republic of Korea

[h] Department of Robotics Engineering, Hanyang University, 55 Hanyangdaehak-ro, Ansan, Gyeonggi-do, 15588, Republic of Korea

ARTICLE INFO

Article history:
Received 31 January 2022
Accepted 3 April 2022
Available online 14 April 2022

Keywords:
B_2O_3 glasses
Er^{3+}
Judd-Ofelt analysis

ABSTRACT

Current work principally provides an idea on controlling the Er^{3+}: NIR (near-infrared) emission characteristics by changing a glass constituent and finding a suitable glass host favorable to design a novel C-optical band (1.53–1.565 μm) amplifier. By melting and rapid quench route, six transparent Er^{3+} (1 mol%)-doped B_2O_3-rich glasses having different single and mixed alkali ions were fabricated, and optical and fluorescence (visible and NIR) traits including Er^{3+} ion upper-levels $^4S_{3/2}$ and $^4I_{13/2}$ decay dynamics were inspected for such samples. At 1.4–1.65 μm wavelength range, an intense and wide NIR luminescence band centered at 1.532 μm (Er^{3+}: $^4I_{13/2} \rightarrow {}^4I_{15/2}$ transition) has been obtained by a 980 nm laser diode pumping ($^4I_{15/2} \rightarrow {}^4I_{11/2}$). NIR fluorescence $\Delta\lambda_{eff}$ (effective bandwidth) varied

* Corresponding author.
** Corresponding author.
*** Corresponding author.
**** Corresponding author.
E-mail addresses: gandham@knu.ac.kr (G. Lakshminarayana), dolee@knu.ac.kr (D.-E. Lee), yooncsmd@gmail.com (J. Yoon), taejoon@hanyang.ac.kr (T. Park).

https://doi.org/10.1016/j.jmrt.2022.04.012

Fluorescence characteristics
CIE color coordinates
C-optical band amplifier

depending on added single or mixed alkali ions, and a maximum $\Delta\lambda_{eff}$ ~74.66 nm was acquired for Er^{3+}: Li ions constituting glass. For the $^4I_{13/2} \rightarrow {}^4I_{15/2}$ transition, σ_{emi} (stimulated emission cross-section) was evaluated using both Füchtbauer–Ladenburg and McCumber's theories. In all glasses, comparably, higher gain bandwidth (= 5.384×10^{-26} cm^3) and peak σ^M_{emi} (= 1.692×10^{-20} cm^2) values have been attained for $^4I_{13/2} \rightarrow {}^4I_{15/2}$ transition in Li ions containing sample, and also this glass possesses the largest σ_{abs} (absorption cross-section) (= 1.459×10^{-20} cm^2) for $^4I_{15/2} \rightarrow {}^4I_{13/2}$ transition. Further, at distinctive P (population inversion) values, gain spectra were computed, and all samples show C-optical band amplification beginning from P = 50%. All analyzed NIR fluorescence results indicate that Li ions having glass could be a potential gain medium for fiber amplifiers.

1. Introduction

By many research groups, for the past few decades onwards rare-earth (RE)-doped inorganic materials like phosphors, glasses, single crystals, and ceramics have been under extensive investigation for such materials possible utilization in solid-state lighting [1,2], lasers [3–6], fiber amplifiers [7–9], bioimaging *via* up-conversion [10,11], and solar cells *via* down-conversion [12,13] owing to RE-ions' high fluorescence intensity, lasing emissions with large cross-sections, and high conversion efficiency that involves usually the f–f transitions of their unique electronic energy levels. Considering the low cost, easy synthesis process, wide compositional ranges, and moderate to possible higher RE ion doping levels with wide non-homogeneous luminescence bands, glasses could be a better choice for fiber lasers and amplifiers application [[7–9], [14,15]]. Vitally visible, NIR (near-infrared), and MIR (mid-infrared) emission features and related stimulated emission cross-sections (σ_{emi}) of a specific RE ion depends largely on selected glass host composition and its phonon energy or hydroxyl content [16]. For RE ions doping, there exist various kinds of glass hosts such as B_2O_3, SiO_2, P_2O_5, GeO_2, and TeO_2-based ones, while Bi_2O_3, Sb_2O_3, and V_2O_5 could also act as glass formers under certain conditions. In addition, fluoride [17], oxyfluoride [18], chalcohalide [19], and chalcogenide/sulfide [20] glasses are also promising for fiber amplifiers and MIR laser sources owing to their low-phonon energy that leads to minimal non-radiative (NR) relaxation rates.

In all trivalent RE activator ions Er^{3+} is widely popular owing to its NIR emissions at ~0.85 μm ($^4S_{3/2} \rightarrow {}^4I_{13/2}$), ~1.25 μm ($^4S_{3/2} \rightarrow {}^4I_{11/2}$), ~1.53 μm ($^4I_{13/2} \rightarrow {}^4I_{15/2}$), and ~1.7 μm ($^4S_{3/2} \rightarrow {}^4I_{9/2}$), and MIR emissions at ~2.8 μm ($^4I_{11/2} \rightarrow {}^4I_{13/2}$), ~3.3 μm ($^4S_{3/2} \rightarrow {}^4F_{9/2}$), and ~3.5 μm ($^4F_{9/2} \rightarrow {}^4I_{9/2}$) including upconversion luminescence at ~0.66 μm ($^4F_{9/2} \rightarrow {}^4I_{15/2}$), ~0.55 μm ($^4S_{3/2} \rightarrow {}^4I_{15/2}$), and ~0.525 μm ($^2H_{11/2} \rightarrow {}^4I_{15/2}$) [21]. Especially as Er^{3+}: NIR luminescence centered at ~1.53 μm coincides with SiO_2 glass fibers low-loss optical communication window, since a few decades EDFAs (Erbium-doped fiber amplifiers) or Er^{3+}-doped glasses and fibers are in use commercially in telecommunications for C-optical band (1.53–1.565 μm) amplification with large-gain and minimal noise [22–26]. Nowadays EDFAs are an integral part of WDM (wavelength division multiplexing) communication systems. Commonly for EDFAs, because of Er^{3+}: $^4I_{9/2}$, $^4I_{11/2}$, and $^4I_{13/2}$ ladder-like energy levels, 1480 nm or 980 nm optical pumping could be utilized where 1480 nm laser excitation gives larger output while 980 nm pumping favors low noise amplification [27]. Other widely utilized RE ions are Yb^{3+}, Nd^{3+}, Pr^{3+}, and Tm^{3+} for their NIR emission transitions around 1 μm, 1.06 μm, 1.3 μm, and 1.47 μm and 1.9 μm accordingly for high power solid-state lasers and fiber amplifiers. Also, Er^{3+}: MIR emissions are useful in laser surgery, defense, eye-safe LIDAR (light detection and ranging), air pollution monitoring, molecular spectroscopy, and remote sensing [28].

Recently, in literature, by various researchers Er^{3+} ion's NIR and/or MIR fluorescence characteristics have been thoroughly studied and reported in different types of glasses like tellurite [29,30], germanate [31], silicate [32], phosphate [33], borate [34], borotellurite [35], antimony [36], oxyfluoride [37], fluoride [38], chalcogenide [39], and fluorochloride [40] glasses for relevant photonic applications.

In all distinct kinds of oxide glasses, borate is familiar as a typical network former owing to its favorable traits like large glass formation tendency, lesser fusion heat, higher bond strength, better thermal and mechanical stabilities, small cation size, reasonable RE ion's solubility, and better optical transparency [41,42]. [BØ$_3$] and [BØ$_4$]$^-$ (Ø = bridging oxygen (BO)) are the two basic structural units in all B_2O_3-based glasses where superstructural units like orthoborate, pyroborate, pentaborate, tetraborate, tri-borate, and di-borate groups could also form in the network relying on the added modifiers (*e.g.* alkali/alkaline metal oxides) content [43]. Here the hygroscopic character and large phonon energy (~1400 cm^{-1}) of borates could be reduced by introducing suitable amounts of modifier oxides and/or heavy metal oxides or related fluorides into the glass network [34,44]. Generally, incorporation of F^- ions in higher content depletes the OH^- and reduces phonon energy. As such, B_2O_3-based glasses are found promising for their application in bone regeneration [45], low-*k* microelectronics [46], superionic conductors [47], nonlinear optics [48], nuclear waste immobilization [49], and nuclear radiation shielding [50]. Multicomponent B_2O_3-based glasses exhibit excellent optical transparency up to the NIR region for the production of optical fiber amplifiers when doped with suitable trivalent RE ions

[34]. In a glass network, BaO acts as a modifier and improves the thermal stability of the glass [51], and the B_2O_3–BaO glass system was found useful for frequency-doubling [48,52]. Relying on the added content (low or high) to a glass, ZnO plays either a modifier or a network former role and promotes refractive index and glass-forming range [53,54]. Kim et al. [55] have investigated the electrical and thermal features of B_2O_3–BaO–ZnO glasses for their possible application as dielectric layers in PDPs instead of Pb-based ones. Usually, Li_2O or Na_2O, or K_2O inclusion to a B_2O_3 glass matrix results in distinctive structural rearrangements creating NBOs (non-bridging oxygens), say, BO_3 to BO_4 unit transformation [43,56]. Further, it is known that the higher thermal conductivities (thermal dissipations) of glasses or crystals could increase the performance of the lasers. Generally, the thermal conductivity of oxides containing a smaller cation atomic mass is higher than that of a larger atomic mass cation. In this regard, having the light element B (Boron) with a smaller cation size and atomic mass, B_2O_3-based glasses might possess a better thermal conductivity for improving laser efficiency.

For RE-doped materials, Judd-Ofelt (J-O) theory [57,58] is routinely adopted as an efficient approach to evaluate or predict both absorption and emission bands' oscillator strengths. Here three J-O intensity parameters *i.e.* Ω_λ ($\lambda = 2$, 4, and 6) deduced from absorption spectra could be applied to compute various radiative factors like branching ratios (β_R), transition probabilities (A_R), and radiative lifetimes (τ_{rad}) of different excited states of RE ions in analyzing the luminescence traits of glasses and crystals. Considering RE-doped phosphors, because of the unattainability of absorption spectra for such materials, recently, for achieving J-O parameters of Er^{3+}-doped $NaYF_4$ phosphors Luo et al. [59] have proposed the fluorescence decay method, Zhang et al. [60] have utilized diffuse-reflection spectra in evaluating J-O parameters for β-$NaYF_4$:Er^{3+}/Yb^{3+} phosphors, and Luo et al. [61] have established a method to obtain Ω_2, Ω_4, and $\Omega6$ values from recorded excitation spectra for the synthesized Y_2O_3:Er^{3+} nanocrystals, NGW: Er powders, and YLF: Nd powders.

To consider RE-doped materials *i.e.* glasses or phosphors or glass-ceramics for potential solid-state lighting applications, primarily, evaluating the CIE (Commission Internationale de l'éclairage) (x, y) values and CP (color purity) from CIE values using their visible fluorescence spectra is crucial [44,54].

Given this context, in this work, we intend to examine the visible and NIR fluorescence features of 1 mol% Er^{3+}-doped B_2O_3-rich glasses mainly for application in C-optical band amplification. Here optical traits were studied with varied single or mixed alkali oxides content. Visible luminescence and Er^{3+}: $^4S_{3/2}$ level decay times have been attained under UV light pumping. NIR fluorescence and decay times were acquired upon 980 nm LD (laser diode) excitation. All samples exhibit emissions centered at 0.55 μm and 1.532 μm. J-O parameters, and A_R, τ_R, and β_R of excited levels of Er^{3+} ion have been calculated from absorption and luminescence spectra. σ^{em}_{max} (peak stimulated emission cross-section), $\Delta\lambda_{eff}$ (effective bandwidth), and η (quantum efficiency) have been derived for $^4I_{13/2} \rightarrow {}^4I_{15/2}$ emission transition.

2. Experimental

2.1. Synthesis

With nominal compositions of 49 B_2O_3–10 BaO–10 ZnO–10 LiF– *a* Li_2O–*b* Na_2O–*c* K_2O–1.0 Er_2O_3 (mol %) (where $a = 20$, $b = 0$, $c = 0$; $a = 0$, $b = 20$, $c = 0$; $a = 0$, $b = 0$, $c = 20$; $a = 10$, $b = 10$, $c = 0$; $a = 0$, $b = 10$, $c = 10$; and $a = 10$, $b = 0$, $c = 10$), as presented in Table 1, six Er^{3+}-doped borate-rich glasses in the air atmosphere have been fabricated *via* a familiar melt-quench approach. All chemicals bought from Sigma–Aldrich like B_2O_3 (99.98%), $BaCO_3$ (99.98%), ZnO (99.99%), anhydrous LiF (≥99.99%), Li_2CO_3 (99.99%), Na_2CO_3 (≥99.5%), K_2CO_3 (≥99%), and Er_2O_3 (99.9%) have been used for sample synthesis. Here for K_2O, Na_2O, Li_2O, and BaO oxides, we utilized proper amounts of K_2CO_3, Na_2CO_3, Li_2CO_3, and $BaCO_3$ in corresponding gravimetric factors of 1.467, 1.71, 2.473, and 1.287. Synthesized all six samples were coded as S1, S2, S3, S4, S5, and S6 separately for convenience (see Table 1). Initially, relying on respective glass's composition (mol%), portions of acquired powder chemicals for 20 g batch have been correctly weighed using a microbalance and then intently for 1 h well-mixed and ground evenly. Next, by heating each glass chemical mixture at 950 °C for 30 min in an electric furnace utilizing high purity Al crucibles with closed lids, molten liquids were obtained. At this relatively lesser melting time and temperature operation, the impact of Al_2O_3 inclusion from the crucible could be neglected. Though Boron melts at ~2076 °C, its oxide B_2O_3 melts at ~450 °C. Here, while assuring the quality of the samples, melting time and temperature should be optimized like in our case to make insignificant the glass constituents' evaporation and glass melt corrosion on the crucible. During heating, each molten liquid was periodically stirred by a glass rod to make it bubble-free and clear. Then, such obtained refined molten liquids have been rapidly cast onto a steel plate and pressed by another similar one. As-synthesized samples were straightaway annealed at 350 °C/5 h in a muffle furnace to eliminate thermal stress caused by the quick quenching process and also to enhance mechanical strength. Lastly, all

Table 1 – Nominal chemical composition of the synthesized glasses (mol %).

Sample code	B_2O_3	BaO	ZnO	LiF	Li_2O	Na_2O	K_2O	Er_2O_3
S1	49	10	10	10	20	0	0	1.0
S2	49	10	10	10	0	20	0	1.0
S3	49	10	10	10	0	0	20	1.0
S4	49	10	10	10	10	10	0	1.0
S5	49	10	10	10	0	10	10	1.0
S6	49	10	10	10	10	0	10	1.0

glasses were naturally cooled to ambient temperature by turning off the furnace. Prepared all samples appeared in pink color due to Er^{3+} ion doping. For optical features investigation, all annealed S1–S6 samples have been cut and polished optically with distinct grades of emery papers on both sides, while for XRD (X-ray diffraction), a minor section of each glass was ground separately to fine powders. Photograph of all S1–S6 samples polished to a thickness of 1.5 mm is exhibited in Fig. 1 (a) (see Table 2).

2.2. Measurements

For all S1–S6 samples, thickness, density (ρ) (±0.001 g/cm^3), and refractive index (error: ± 0.001) have been measured using digital Vernier caliper gauge, *via* Archimedes's principle with toluene (99.9%) as a reference liquid, and Abbe refractometer at 589.3 nm accordingly. Kinds of equipment and conditions applied for all S1–S6 samples XRD (10°–80° (2θ) span), absorption (200–2000 nm range), visible emission and excitation spectra, and Er^{3+}: $^4S_{3/2}$ level decay time experiments have been the same as we have given in earlier works [9,54] thus those details are not restated here. For instance, XRD patterns were attained using an Ital Structure APD 2000 diffractometer with Cu-Kα (λ = 1.5418 Å) radiation. Here, at 20 mA anode current and 40 kV voltage, the X-ray tube was wielded, and scattered X-rays intensity was registered *via* a scintillation detector. NIR fluorescence spectra at 1400–1650 nm wavelength range and $^4I_{13/2}$ level decay times were registered by an FLS1000 fluorescence spectrometer (Edinburgh Instruments, UK) under 980 nm pulsed LD excitation (direct pumping from Er^{3+}: $^4I_{15/2}$ state to $^4I_{11/2}$ level) and equipped with a NIR-PMT (InGaAs) detector cooled by LN_2 (liquid nitrogen). During all the optical tests, for getting comparable results, related all experimental terms were invariably maintained and conducted at ambient temperature. All data have been analyzed employing Origin software.

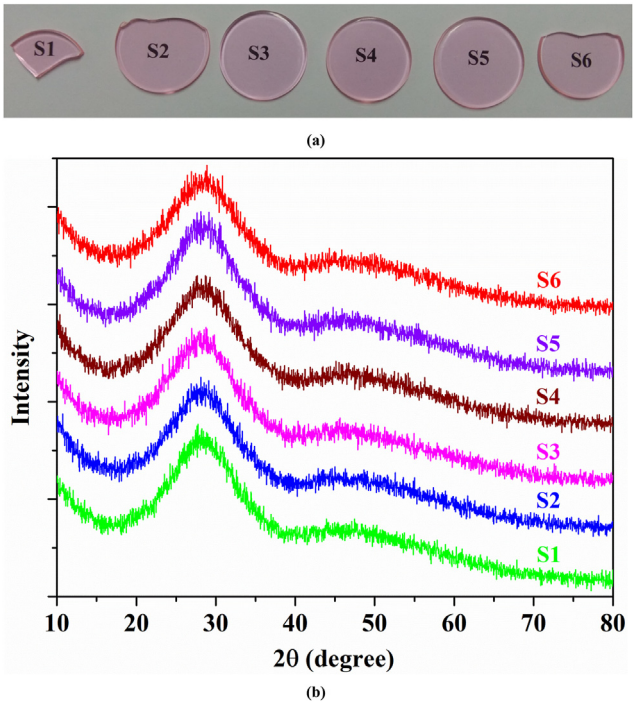

Fig. 1 – (a) Photograph of all the studied glasses (b) X-ray diffraction (XRD) profiles of all the prepared glasses.

3. Results and discussion

3.1. XRD results

In Fig. 1 (b), for all S1–S6 samples, XRD profiles at $10° \leq 2\theta \leq 80°$ span are presented. As anticipated, from XRD patterns which have similar shapes, only two broad humps at 2θ = 17°–38° and 38°–67° extents are identified as evidence of all inspected glasses' non-crystalline state. Here nonexistence of any distinctive sharp peaks affirms that samples are amorphous in character *i.e.*, no atoms arrangement in long-range order and possess no crystalline phases.

3.2. Physical traits

Table 2 (a) supplies some intrinsic characteristics of Er^{3+}, K^+, Na^+, Li^+, Zn^{2+}, Ba^{2+}, and B^{3+} cations present in all S1–S6 glasses. Here *r* (ionic radius) varies conditional on *CN* (coordination number) which leads to the change in *F* (Field strength) also for all cations (http://www.mrl.ucsb.edu/~seshadri/Periodic/). *CN* as 6 is common for all cations present in the studied samples. Here for B^{3+} ion, $r = 0.27$ Å for $CN = 6$, for Ba^{2+} ion, $r = 1.35$ Å for $CN = 6$, for Zn^{2+} ion, $r = 0.74$ Å for $CN = 6$, for Li^+ ion, $r = 0.76$ Å for $CN = 6$, for Na^+ ion, $r = 1.02$ Å for $CN = 6$, K^+ ion, $r = 1.38$ Å for $CN = 6$, for Er^{3+} ion, $r = 0.89$ Å for $CN = 6$, and for O^{2-} anion, $r = 1.40$ Å for $CN = 6$. Table 2 (b) presents various physical factors of all S1–S6 samples derived by utilizing ρ and n (refractive index) values. Relevant formulae utilized to acquire Table 2 (b) data can be found elsewhere [62]. For all samples, depending on molecular weight, ρ is correlatedly changed. As one can notice, V_m (molar volume) also varied (23.724–27.334 cm^3/mol range) similarly to the ρ drift. Slight increase in V_m with different alkali oxides content could be owing to the addition of larger K^+ (1.37 Å) or Na^+ (0.99 Å) in place of smaller Li^+ (0.59 Å).

Usually, relying on bond lengths' increment due to distinct structural units rearrangement in the glass network, V_m increases. An inflate in V_m hints at NBOs (nonbridging oxygens) rise and subsequently a loosely packed network. OPD (oxygen packing density) decreased for all studied samples following the added alkali ions' *r*, representing associated changes in the 'O' (Oxygen) atoms number. Here glass S1 (Li-ions comprising one) has the highest OPD while sample S3 (K- ions constituting one) owns the lowest OPD. Here we did not vary Er^{3+} concentration, but alterations done by different network (alkali ion) contents incorporation. For all samples similar to ρ and n changes, both R_m (Molar refractivity) and α_m (Molar polarizability) improved indicating more BO_4 groups formation in the network causing higher NBOs. Identical to the OPD trend, *M* (Metallization criterion) value reduced slightly for all samples (0.6291–0.6186 span) and is found to be < 1 signifying all S1–S6 glasses' insulating character. E_g (energy gap) value reduced at 7.915–7.654 eV range and R_L (Reflection loss) value enhanced at 6.213–6.551% span depending on introduced single or

Table 2a – The intrinsic characteristics of the different cations present in the studied glasses.

Cations	B^{3+}	Ba^{2+}	Zn^{2+}	Li^{+}	Na^{+}	K^{+}	Er^{3+}
Structural role	Glass former	Glass modifier	Glass modifier	Glass modifier	Glass modifier	Glass modifier	Dopant ion
Coordination number (CN)	3, 4, 6	6, 7, 8, 9, 10, 11, 12	4, 5, 6, 8	4, 6, 8	4, 6, 8	4, 6, 8	6, 8
Cation oxidation number (Z)	3	2	2	1	1	1	3
Ionic radius, r (Å)	0.01 (C N. = 3, 3^+ charge); 0.11 (C N. = 4, 3^+ charge); 0.27 (C N. = 6, 3^+ charge)	1.35 (C N. = 6, 2^+ charge); 1.38 (C N. = 7, 2^+ charge); 1.42 (C N. = 8, 2^+ charge); 1.47 (C N. = 9, 2^+ charge); 1.52 (C N. = 10, 2^+ charge); 1.57 (C N. = 11, 2^+ charge); 1.61 (C N. = 12, 2^+ charge)	0.60 (C N. = 4, 2^+ charge); 0.68 (C N. = 5, 2^+ charge); 0.74 (C N. = 6, 2^+ charge); 0.90 (C N. = 8, 2^+ charge)	0.59 (C N. = 4, 2^+ charge); 0.76 (C N. = 6, 2^+ charge); 0.92 (C N. = 8, 2^+ charge)	0.99 (C N. = 4, 2^+ charge); 1.02 (C N. = 6, 2^+ charge); 1.18 (C N. = 8, 2^+ charge)	1.37 (C N. = 4, 2^+ charge); 1.38 (C N. = 6, 2^+ charge); 1.51 (C N. = 8, 2^+ charge)	0.890 (C N. = 6, 2^+ charge); 1.004 (C N. = 8, 2^+ charge)
Field strength, $F = Z/r^2$ (Å)^2	30,000 for 0.01 (C N. = 3, 3^+ charge); 247.9339 for 0.11 (C N. = 4, 3^+ charge); 41.1523 for 0.27 (C N. = 6, 3^+ charge)	1.0974 for 1.35 (C N. = 6, 2^+ charge); 1.0502 for 1.38 (C N. = 7, 2^+ charge); 0.9919 for 1.42 (C N. = 8, 2^+ charge); 0.9255 for 1.47 (C N. = 9, 2^+ charge); 0.8657 for 1.52 (C N. = 10, 2^+ charge); 0.8114 for 1.57 (C N. = 11, 2^+ charge); 0.7716 for 1.61 (C N. = 12, 2^+ charge)	5.5556 for 0.60 (C N. = 4, 2^+ charge); 4.3253 for 0.68 (C N. = 5, 2^+ charge); 3.6523 for 0.74 (C N. = 6, 2^+ charge); 2.4691 for 0.90 (C N. = 8, 2^+ charge)	2.8727 (C N. = 4, 2^+ charge); 1.7313 (C N. = 6, 2^+ charge); 1.1815 (C N. = 8, 2^+ charge)	1.0203 (C N. = 4, 2^+ charge); 0.9612 (C N. = 6, 2^+ charge); 0.7182 (C N. = 8, 2^+ charge)	0.5328 (C N. = 4, 2^+ charge); 0.5251 (C N. = 6, 2^+ charge); 0.4386 (C N. = 8, 2^+ charge)	3.7874 (C N. = 6, 2^+ charge); 2.9761 (C N. = 8, 2^+ charge)

Table 2b – Physical parameters of all the prepared glasses.

Property	Sample code					
	S1	S2	S3	S4	S5	S6
Average Molecular Weight (g/mol)	69.985	76.405	82.849	73.195	79.624	76.417
Density, ρ (g/cm^3)	2.950	3.012	3.031	2.944	3.024	2.948
Er^{3+} ion concentration, N_{Er}^{3+} ($\times 10^{20}$ ions/cm^3)	2.5388	2.3744	2.2035	2.4225	2.2874	2.3235
Interionic distance, r_i (Å)	15.793	16.149	16.556	16.041	16.351	16.266
Polaron radius, r_p (Å)	6.3645	6.5081	6.6722	6.4647	6.5896	6.5552
Field strength, F (cm^{-2} $\times 10^{14}$)	7.4063	7.0829	6.7389	7.1784	6.9088	6.9815
Refractive index, n_d	1.664	1.672	1.688	1.675	1.682	1.680
Dielectric constant, ϵ	2.769	2.796	2.849	2.806	2.829	2.822
Optical dielectric constant, $p\frac{dt}{dp}$	1.769	1.796	1.849	1.806	1.829	1.822
Molar volume, V_m (cm^3/mol)	23.724	25.367	27.334	24.862	26.332	25.922
Oxygen packing density, OPD (mol/L)	80.089	74.901	69.511	76.421	72.157	73.298
Molar Refractivity, R_m (cm^{-3})	8.799	9.498	10.424	9.342	9.974	9.796
Metallization criterion, M	0.6291	0.6256	0.6186	0.6242	0.6212	0.6221
Energy gap, E_g (eV)	7.915	7.827	7.654	7.794	7.719	7.740
Reflection loss, R_L (%)	6.213	6.325	6.551	6.367	6.466	6.438
Molar Polarizability, α_m (cm^3 $\times 10^{-24}$)	3.485	3.761	4.128	3.699	3.950	3.879
Glass optical basicity, Λ	0.5240	0.5316	0.5532	0.5278	0.5424	0.5386

mixed alkali ions. Here against both oxides BaO (4.4 eV) and ZnO (3.37 eV), B_2O_3 possesses relatively larger E_g (> 10 eV). In noncrystalline samples like glasses, BG (band gap) is generally connected to the energy gap between VB (valence band) and CB (conduction band), in which CB might be varied conditional on network-forming anions. A small increment in both r_i (interionic distance) and r_p (polaron radius) values and decrement in F (field strength) of studied samples could be owing to the alteration of added alkali ions in them. So the effect of alkali ions could be realized by considering F ($F = \frac{Z}{r_p^2}$) values, where Z = Er ion's valence state. 7.4063, 7.0829, 6.7389, 7.1784, 6.9088, and 6.9815 ($\times 10^{14}$ cm^{-2}) are the F values for S1, S2, S3, S4, S5, and S6 samples respectively. Here F value inversely changed to r_p value relying on added alkali ion (seeTable 2 (b)). Generally, for metal ion bonds, a low F value specifies large ionicity, while high F bonds possess greater covalency.

Further, following the relation given in Ref. [63], calculated Λ (optical basicity) values for all S1–S6 glasses are provided inTable 2 (b). Table 2 (c) presents the X_i (Pauling electronegativity), γ (optical basicity moderating parameter), and Λ values for all cations of S1–S6 samples along with Λ of all glass compounds. Here $\gamma = 1.36\ (X_i - 0.26)$. Λ value minorly increased from Li to Na to K ions addition and was found to be larger for glass S3. Enhancing Λ indicates oxide ions' improving potential to supply electrons to proximate cations with Li to K ions incorporation.

3.3. *Optical absorption*

Fig. 2 (a) depicts UV–Vis–NIR absorption spectra of all S1–S6 samples at 270–1800 nm spectral span. Eleven absorption bands peaked at 364 nm (27,472 cm^{-1}), 378 nm (26,455 cm^{-1}), 406 nm (24,630 cm^{-1}), 451 nm (22,172 cm^{-1}), 487 nm (20,533 cm^{-1}), 521 nm (19,193 cm^{-1}), 544 nm (18,382 cm^{-1}), 651 nm (15,360 cm^{-1}), 798 nm (12,531 cm^{-1}), 974 nm (10,266 cm^{-1}), and 1530 nm (6535 cm^{-1}) assigned to transitions originating from Er^{3+}: $^4I_{15/2}$ ground state to relevant $^4G_{9/2}$, $^4G_{11/2}$, $^2G_{9/2}$, $^4F_{5/2}+^4F_{3/2}$, $^4F_{7/2}$, $^2H_{11/2}$, $^4S_{3/2}$, $^4F_{9/2}$, $^4I_{9/2}$, $^4I_{11/2}$, and $^4I_{13/2}$ excited states [33,34] are identified from Fig. 2 (a). Here $^4I_{15/2} \rightarrow {}^4I_{13/2}$ transition shows both MD (magnetic-dipole) and ED (electric-dipole) contributions, and the rest of them all are ED only in nature. Moreover, in all transitions, $^4I_{15/2} \rightarrow {}^4G_{11/2}$ and $^4I_{15/2} \rightarrow {}^2H_{11/2}$ are proportionally very intense as they obey $\Delta S = 0$, $|\Delta L| \leq 2$, and $|\Delta J| \leq 2$ selection rule as HS (hypersensitive) ones [9,44,54]. Usually, such HS transitions intensity varies considerably depending on Er^{3+} ion's interaction strength with host matrix in a local environment

Table 2c – Glass elements optical basicity properties.

Cation	Electronegativity [X_i]	$\Lambda = (0.75/(X_i - 0.25)$	Oxides			Fluorides		
			Basicity moderating parameter, γ	Oxide	$\Lambda = \gamma^{-1}$	Basicity moderating parameter	Fluoride	$\Lambda = \gamma^{-1}$
B^{3+}	2.04	0.4190	2.4208	B_2O_3	0.4131			
Ba^{2+}	0.89	1.1719	0.8568	BaO	1.1671			
Zn^{2+}	1.65	0.5357	1.8904	ZnO	0.5290			
Li^+	0.98	1.0274	0.9792	Li_2O	1.0212	2.2522	LiF	0.4440
Na^+	0.93	1.1029	0.9112	Na_2O	1.0975			
K^+	0.82	1.3158	0.7616	K_2O	1.3130			
Er^{3+}	1.24	0.7576	1.3328	Er_2O_3	0.7503			

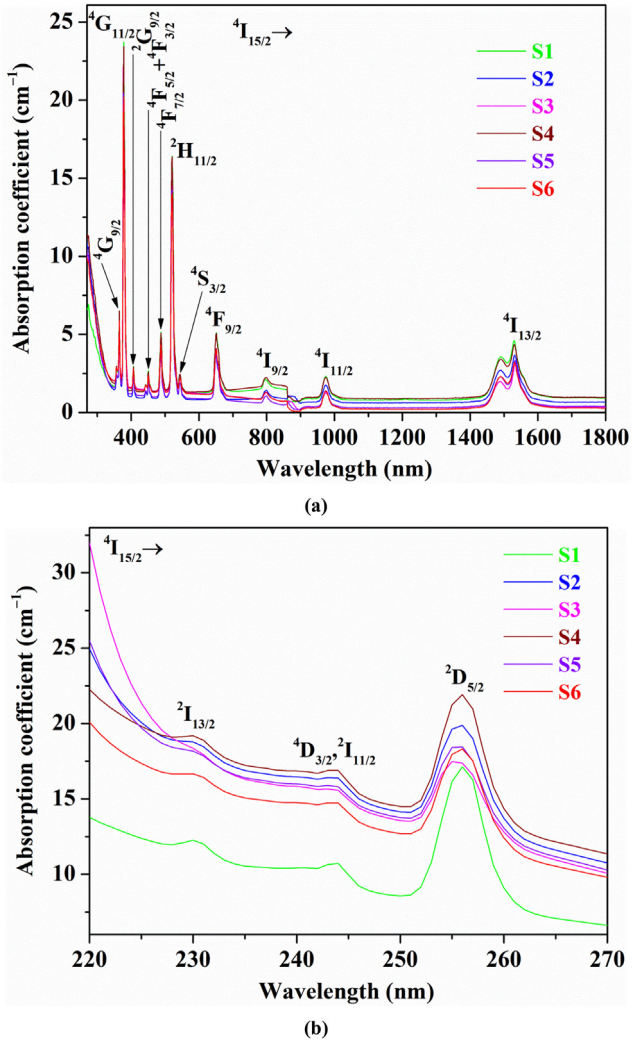

Fig. 2 – (a) UV–Vis–NIR optical absorption spectra (b) UV absorption spectra at 220–270 nm wavelength range for all 1.0 mol% Er^{3+}-doped glasses. Here, the y-axis scale is shown in the absorption coefficient (cm^{-1}) values.

that ultimately affects $\Omega_{2,4,6}$ (J-O parameters) magnitude. At 220–270 nm wavelength span for all S1–S6 glasses, UV absorption spectra are illustrated in Fig. 2 (b). Three intense UV bands peaked at 230 nm (43,478 cm^{-1}), 244 nm (40,983 cm^{-1}), and 256 nm (39,062 cm^{-1}) are noticed from Fig. 2 (b) that could be ascribed to transitions to $^2I_{13/2}$, ($^4D_{3/2}$,$^2I_{11/2}$), and $^2D_{5/2}$ excited states from Er^{3+}: $^4I_{15/2}$ ground state accordingly [64].

3.4. *Optical band gaps and urbach energy*

For all S1–S6 glasses, utilizing relevant formulae stated in Refs. [54,62], from UV absorption spectra, ΔE (Urbach energy), different E_{opt} (optical band gap) values such as indirect forbidden, direct forbidden, indirect allowed, direct allowed, experimental E_{opt} from 'κ' (extinction coefficient), and E_{opt} by ASF (absorption spectrum fitting) procedure including λ_{edge} (cut-off wavelengths) are evaluated. All obtained such outcomes are provided in Table 3 and related plots are shown in Figs. S1 (a-h) in Supplementary material (SM).

Table 3 – Fundamental absorption edge (λ_{edge} ± 0.05 nm), direct optical band gap (E_{opt} ± 0.005 eV), indirect optical band gap (E_{opt} ± 0.005 eV), direct forbidden optical band gap (E_{opt} ± 0.005 eV), indirect forbidden optical band gap (E_{opt} ± 0.005 eV), optical band gap evaluated through ASF method (E_{opt}^{ASF} ± 0.005 eV), optical band gap from the extinction coefficient (E_{opt} from 'κ' ± 0.005 eV), Urbach energy (ΔE ± 0.002 eV), and two photon absorption coefficient (TPA) (β ± 0.005 cm/GW) of all the S1–S6 glasses.

Sample Code	λ_{edge} (nm)	Direct optical band gap (eV) (n = 1/2)	Indirect optical band gap (eV) (n = 2)	Direct forbidden band gap (eV) (n = 3/2)	Indirect forbidden band gap (eV) (n = 3)	$(1/\lambda_g)$ (nm^{-1}) (± 1× 10^{-6} nm^{-1})	λ_g (nm) (± 1× 10^{-6} nm)	Optical band gap E_{opt}^{ASF} (eV)	E_{opt} from 'κ' (eV)	Urbach energy ΔE (eV)	β (cm/GW)
S1	330	4.031	3.832	4.022	3.875	0.003042	328.73	3.772	3.894	0.406	5.721
S2	333	4.019	3.810	4.017	3.821	0.002999	333.44	3.719	3.867	0.415	5.899
S3	344	3.983	3.713	3.989	3.749	0.002952	338.75	3.661	3.765	0.440	6.685
S4	334	4.005	3.798	4.010	3.809	0.002981	335.46	3.696	3.834	0.421	5.996
S5	337	3.995	3.738	4.002	3.784	0.002967	337.04	3.679	3.803	0.437	6.482
S6	346	3.974	3.701	3.981	3.718	0.002935	340.72	3.639	3.728	0.442	6.782

Concisely, as indicated in Ref. [62]:

$$\alpha(v) = B \times \frac{(hv - E_{opt})^r}{hv} \quad (1)$$

where $h\nu$ = photon energy, r = 1/2, 2, 3/2, and 3 individually for transitions direct, indirect, direct forbidden, and indirect forbidden, and B (band-tailing parameter) = constant.

$$\text{Here } \alpha(\lambda) = 2.303 \times O.D./t \quad (2)$$

where t = sample thickness (in cm), $O.D.$ = optical density.

Likewise, as mentioned in Ref. [54]:

$$E_{opt}^{ASF} = \frac{1240}{\lambda_g} \quad (3)$$

where λ_g = wavelength associated with E_{opt}.

Also, as given in Ref. [54]:

$$\alpha = \frac{4\pi\kappa}{\lambda} \quad (4)$$

Here experimental E_{opt} could be acquired from 'κ' against $h\nu$ graphs.

Further, as stated in Refs. [54,62]:

$$\alpha(\nu) = \alpha_0 \exp\left(\frac{h\nu}{\Delta E}\right) \quad (5)$$

where α_0 = constant and ΔE = Urbach energy

Here ΔE = 1/slopes of ln(α) vs $h\nu$ graphs' linear parts.

As can be noticed from Table 3, λ_{edge} value changes at 330–346 nm span having increasing trend for single or mixed alkali ions. All obtained values of E_{opt} reduce from S1 to S3 sample and S4 to S6 glass hinting at structural changes occurrence in such glasses *i.e.* higher NBOs creation over BOs.

The range of *Eopt* (direct allowed) values derived at 3.974–4.031 eV is found to be greater than those of $25Li_2O$–$15Bi_2O_3$-(45-x)B_2O_3–$15TeO_2$-xEr_2O_3 (x = 0.1, 0.5, 1, 2 mol %) (2.70–2.77 eV range) [35], (65-x)H_3BO_3+10MgO+5PbO+$15CaF_2$-+5ZrO_2+xEr_2O_3 (x = 0.05, 0.1, 0.3, 0.5, 1, 2 wt.%) (3.299–3.365 eV span) [65], and (65–x)B_2O_3–$5Na_2O$–10PbO–5ZnO –$5Li_2$-O–xEr_2O_3 (x = 0.05, 0.1, 0.5, 1.0, 2.0, 4.0 mol%) (3.735–3.824 eV extent) [66] glasses and smaller than that of (20-x)Na_2SO_4-–20PbO–$60P_2O_5$-xEr_2O_3 (x = 0.1, 0.3, 0.5, 0.7, 1.0 mol%) (4.798–4.957 eV range) glasses [67], indicating that comparably all S1–S6 glasses could have lesser intrinsic defects in their network structure than those of glasses reported in Refs. [35,65,66] as generally, the higher the defects, the lower the E_{opt} [65].

Since indirect transitions are situated at lesser energy than the direct ones, all S1–S6 glasses could be categorized as non-direct materials. Moreover, E_{opt} from 'κ' matches well with E_{opt} values for m = 3 transitions for all samples, so E_{opt} originates distinctly because of indirect transitions. Next, ΔE varies at 0.406–0.442 eV range similarly to λ_{edge} drift and increasing ΔE specifies improving disorderness in samples with changing alkali (single or mixed) content.

From E_{opt} and TPA (two-photon absorption) coefficient (β) linear link [68] as:

$$\beta \text{ (cm/GW)} = 36.76 - 8.1\ E_{opt} \text{ (eV)} \quad (6)$$

obtained β values applying E_{opt} (indirect) are given in Table 3.

Here, possessing minimal β (= 5.721 cm/GW), glass S1 is more suitable for nonlinear optical devices fabrication [69].

3.5. *Judd-Ofelt (J-O) analysis*

For all S1–S6 samples, considering all identified transitions from Fig. 2 (a), f_{exp} (experimental oscillator strength), Ω_2, Ω_4, and Ω_6 parameters, f_{cal} (calculated oscillator strength), and δ_{rms} variations for f_{exp} and f_{cal} are evaluated applying the J-O model [57,58]. Obtained all outcomes are depicted in Table 4. For J-O parameters computation, the values of reduced matrix elements, U^{t2} (t = 2, 4, 6) were taken from Ref. [70] (see Table S1 in SM). Employed customary formulae utilized for J-O analysis can be found elsewhere [71,72]. Here obtained δ_{rms} quantities are in agreeable limit hinting at the J-O model calculation method's validity. Uncertainties related to Ω_2, Ω_4, and Ω_6 have been calculated straightforwardly from the J-O fit taking into account the residual values of calculated and measured intensities. Here for all samples except for S2, J-O parameters show Ω_2>Ω_6>Ω_4 trend while for glass S2 Ω_2>Ω_4>Ω_6 course is noticed. Both Ω_4 and Ω_6 are insensitive to the glass structural changes, and they rely on the wave function's radial part and highly on host matrix optical basicity [73]. Here, specifically, Ω_6 is inversely proportional to the Er–O bonds' covalency, which can be tuned by the glass host composition, whereas Ω_4 reflects the glass matrix's viscosity and rigidity. In this regard, Ω_4>Ω_6 found for sample S2 than the rest of the samples' Ω_6>Ω_4 trend indicates a higher rigidity of glass S2 structure than them. Generally, Ω_2 is sensitive to the asymmetry in the RE ions' vicinity (short-range effects), and the variations in Ω_6 correspond to the glass host's long-range effects. Ω_2 could also represent the covalence between ligand anions and RE ions [73]. For all S1–S6 samples, Ω_2 is higher than Ω_4 and Ω_6 indicating a greater degree of Er–O bond covalency and Er^{3+} sites' asymmetry. Usually, Er–F bond is more ionic than Er–O bond as F possesses larger electronegativity (3.98) than O (3.44) element. Further, Ω_2 slightly increases for single alkali ions from Li to Na to K (S1 to S3) while it is reduced for mixed alkali ions in the order S4>S5>S6. Here, from S4 to S6 sample, the gradual reduction in Ω_2 value with varying mixed alkali oxides content as Li_2O/Na_2O (S4), Na_2O/K_2O (S5), and Li_2O/K_2O (S6) could be owing to the persistent structural modifications' occurrence from S4 to S6 glass with ascendancy in the enhancing local environment's regularity over the nature of bonding. A larger value of Ω_2 arises from the correlatively dominant oscillator strength of Er^{3+}: $^4I_{15/2} \rightarrow {}^4G_{11/2}$ and $^2H_{11/2}$ HS transitions also. Comparably higher Ω_2 for glass S3 in all samples indicates a lesser symmetry at Er^{3+} ion sites vicinity when K_2O is added. Also, both Ω_4 and Ω_6 values are low for sample S3 in all glasses specifying its lower mechanical features with decreased rigidity of glass structure.

Table 5 displays Ω_2, Ω_4, and Ω_6 values and such values trend obtained for sample S3 against distinct reported Er^{3+}-doped glass systems [16, 18, 29, 31–35, 65, 66, 73]. Ω_2 for glass S3 is noticed to be higher than those of (mol%) $50TeO_2$–$39ZnF_2$–9ZnO–1ZnS–$1ErF_3$ [16], $68TeO_2$–$5Ga_2O_3$-–$10BaF_2$–$11AlF_3$–$4Y_2O_3$–$2ErF_3$ [18], $98TeO_2$–$2Er_2O_3$ [29], $65GeO_2$–$12Ga_2O_3$–23(BaF_2 + La_2O_3 + Li_2O)–$0.5Er_2O_3$ [31],

Table 4 – Absorption band assignments (from the ground state, $^4I_{15/2}$), experimental ($f_{exp} \times 10^{-6}$ cm^2), and calculated ($f_{cal} \times 10^{-6}$ cm^2) oscillator strengths of all 1.0 mol% Er^{3+}-doped glasses along with J-O parameters. Wavelengths correspond to average transition energies.

Sample code			S1		S2		S3		S4		S5		S6	
Transition		λ (nm)	f_{exp}	f_{cal}	f_{exp}	f_{cal}	f_{exp}	f_{cal}	f_{exp}	f_{cal}	f_{exp}	f_{cal}	f_{exp}	f_{cal}
$^4I_{15/2}\rightarrow$														
	$^4I_{13/2}$	1518	5.10 4.57 ed 0.53md[a]	4.92	4.26 3.72 ed 0.54md[a]	4.10	3.86 3.32 ed 0.54md[a]	3.72	4.88 4.35 ed 0.53md[a]	4.71	4.15 3.61 ed 0.54md[a]	4.00	4.24 3.70 ed 0.54md[a]	4.09
	$^4I_{11/2}$	979	1.68	2.26	1.41	1.93	1.27	1.80	1.60	2.18	1.36	1.89	1.42	1.91
	$^4I_{9/2}$	805	1.28	0.95	1.04	0.88	0.80	0.71	1.24	0.96	0.86	0.77	0.88	0.78
	$^4F_{9/2}$	655	6.47	6.71	5.74	5.90	4.87	4.99	6.40	6.62	5.30	5.43	5.41	5.54
	$^4S_{3/2}$	546	1.06	1.91	0.95	1.56	0.89	1.42	1.08	1.81	0.92	1.54	0.90	1.58
	$^2H_{11/2}$	522	20.95	20.92	21.34	21.31	21.16	21.13	21.84	21.81	20.17	20.15	19.33	19.30
	$^4F_{7/2}$	488	5.52	7.28	4.97	6.11	4.34	5.43	5.55	7.01	4.64	5.89	4.80	6.03
	$^4F_{5/2,3/2}$	450	2.40	3.66	2.03	3.00	1.74	2.74	2.38	3.48	1.84	2.96	1.97	3.04
	$^2G_{9/2}$	407	2.25	2.79	2.04	2.32	1.82	2.09	2.25	2.67	1.80	2.26	1.84	2.32
	$^4G_{11/2}$	379	39.64	37.02	40.09	37.71	40.78	37.37	41.15	38.58	38.14	35.65	36.61	34.16
	$^4G_{9/2}$	363	7.96	4.36	7.38	3.89	6.88	3.24	8.01	4.33	6.84	3.52	6.78	3.59
RMS deviation, δ_{rms} ($\times$ 10^{-6})			1.539		1.378		1.588		1.497		1.381		1.344	
J - *O* parameters ($\times$ 10^{-20} cm^2)														
Ω_2			11.959 ± 0.048		12.410 ± 0.0235		12.606 ± 0.0607		12.463 ± 0.027		11.792 ± 0.063		11.186 ± 0.056	
Ω_4			4.035 ± 0.081		3.749 ± 0.038		2.927 ± 0.100		4.077 ± 0.048		3.210 ± 0.107		3.262 ± 0.100	
Ω_6			4.565 ± 0.298		3.721 ± 0.256		3.346 ± 0.251		4.304 ± 0.286		3.643 ± 0.265		3.743 ± 0.257	

[a] Magnetic dipole (md) oscillator strength was subracted from experimental oscillator strength for J-O analysis.

$50SiO_2–30Li_2O–18CdO\text{-}1Gd_2O_3–1Er_2O_3$ [32], $60P_2O_5–10Al_2O_3–30Na_2O–1Er_2O_3–5LiF$ [33], $10Li_2O–10PbO–9Al_2O_3–70B_2O_3–1Er_2O_3$ [34], $25Li_2O–15Bi_2O_3–44B_2O_3–15TeO_2–1Er_2O_3$ [35], 1ErZMB [65], $64B_2O_3–15Na_2O–10PbO–5ZnO–5Li_2O–1Er_2O_3$ [66], and $75B_2O_3–25Na_2O\text{-}0.3Er_2O_3$ [73] glasses related values, specifying that sample S3 possesses lesser symmetry at Erbium ion sites place and higher degree of covalency between Erbium ions and proximate ligands than in them. For sample S3 identified Ω_2, Ω_4, and Ω_6 tendency is similar to some other studied Er^{3+}: borate glasses trend like $10Li_2O–10PbO–9Al_2O_3–70B_2O_3–1Er_2O_3$ [34], $25Li_2O–15Bi_2O_3–44B_2O_3–15TeO_2–1Er_2O_3$ [35], and 1ErZMB [65] (see Table 5). In all compared samples, $50SiO_2–30Li_2O–18CdO\text{-}1Gd_2O_3–1Er_2O_3$ glass [32] only owns $\Omega_4>\Omega_2>\Omega_6$ trend. Here, in distinct hosts Ω_2, Ω_4, and Ω_6 change is owing to intermediates and modifiers and existence of Er^{3+} ions in different site symmetry.

3.6. *Visible fluorescence*

For all S1–S6 samples, Fig. 3 (a) shows excitation spectra within 260–530 nm extent recorded at $\lambda_{emi.} = 550$ nm. Here, excitation spectra are useful to identify suitable wavelengths, which can be utilized later for an effective optical pumping of the samples. Usually, the wavelength related to an intense excitation peak gives strong emissions. Eight bands peaked at 356 nm (28,089 cm^{-1}), 363 nm (27,548 cm^{-1}), 376 nm (26,595 cm^{-1}), 405 nm (24,691 cm^{-1}), 441 nm (22,675 cm^{-1}), 449 nm (22,271 cm^{-1}), 486 nm (20,576 cm^{-1}), and 520 nm (19,230 cm^{-1}) are found in all samples and can be assigned to

Table 5 – Comparison of Judd-Ofelt intensity parameters (Ω_λ, $\times$ 10^{-20} cm^2) and their trend of glass S3 with different Er^{3+}-doped glass systems.

Glass system	Ω_2	Ω_4	Ω_6	Trends of Ω_λ	Reference
Glass S3	12.606	2.927	3.346	$\Omega_2>\Omega_6>\Omega_4$	Present work
$50TeO_2–39ZnF_2–9ZnO–1ZnS–1ErF_3$ (mol%) glass	4.01	1.50	1.16	$\Omega_2>\Omega_4>\Omega_6$	[16]
$68TeO_2–5Ga_2O_3–10BaF_2–11AlF_3–4Y_2O_3–2ErF_3$ (mol%) glass	5.49	1.91	1.07	$\Omega_2>\Omega_4>\Omega_6$	[18]
$98TeO_2–2Er_2O_3$ (mol%) glass	4.025	1.506	0.603	$\Omega_2>\Omega_4>\Omega_6$	[29]
$65GeO_2–12Ga_2O_3–23(BaF_2 + La_2O_3 + Li_2O)–0.5Er_2O_3$ (mol%) glass	4.74	1.89	0.82	$\Omega_2>\Omega_4>\Omega_6$	[31]
$50SiO_2–30Li_2O–18CdO\text{-}1Gd_2O_3–1Er_2O_3$ (mol%) glass	2.927	4.231	0.628	$\Omega_4>\Omega_2>\Omega_6$	[32]
$60P_2O_5–10Al_2O_3–30Na_2O–1Er_2O_3–5LiF$ (mol%) glass	4.08	1.37	0.93	$\Omega_2>\Omega_4>\Omega_6$	[33]
$10Li_2O–10PbO–9Al_2O_3–70B_2O_3–1Er_2O_3$ (mol%) glass	4.35	0.26	2.29	$\Omega_2>\Omega_6>\Omega_4$	[34]
$25Li_2O–15Bi_2O_3–44B_2O_3–15TeO_2–1Er_2O_3$ (mol%) glass	9.01	1.98	2.87	$\Omega_2>\Omega_6>\Omega_4$	[35]
1ErZMB glass	5.56	1.44	2.15	$\Omega_2>\Omega_6>\Omega_4$	[65]
$64B_2O_3–15Na_2O–10PbO–5ZnO–5Li_2O–1Er_2O_3$ (mol%) glass	6.19	5.68	0.13	$\Omega_2>\Omega_4>\Omega_6$	[66]
$75B_2O_3–25Na_2O\text{-}0.3Er_2O_3$ (mol%) glass	6.11	1.66	0.99	$\Omega_2>\Omega_4>\Omega_6$	[73]

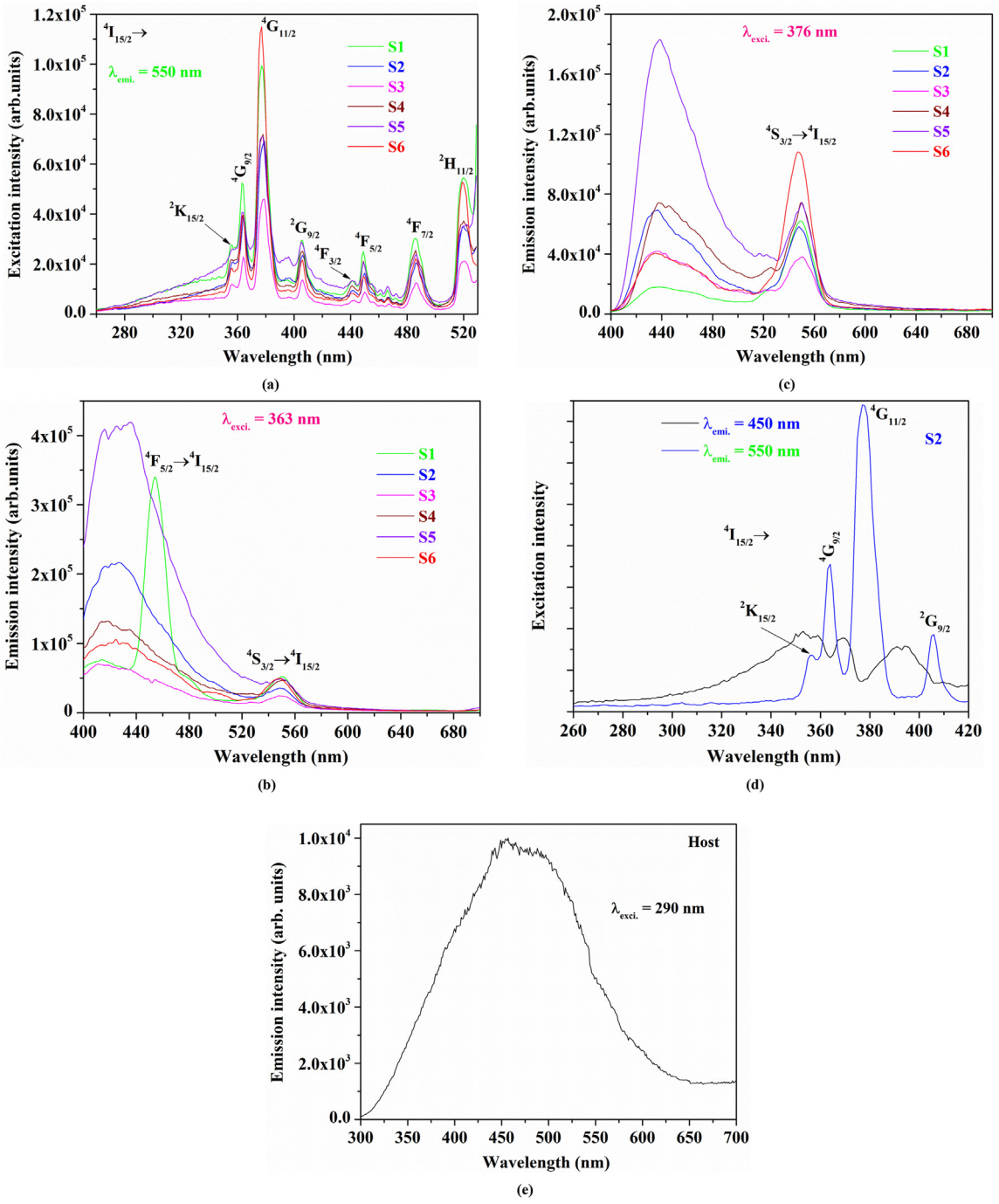

Fig. 3 – (a) Photoluminescence excitation spectra of all the 1.0 mol% Er^{3+}-doped glasses by monitoring emission at 550 nm. Photoluminescence spectra of all the 1.0 mol% Er^{3+}-doped glasses under (b) 363 nm and (c) 376 nm excitation wavelengths. (d) Excitation spectra at $\lambda_{emi.}$ = 450 nm and $\lambda_{emi.}$ = 550 nm of glass S2. (e) Emission spectrum of the host glass under 290 nm excitation.

transitions from Er^{3+}: $^4I_{15/2}$ state to $^2K_{15/2}$, $^4G_{9/2}$, $^4G_{11/2}$, $^2G_{9/2}$, $^4F_{3/2}$, $^4F_{5/2}$, $^4F_{7/2}$, and $^2H_{11/2}$ upper levels individually [34]. In all such peaks, an intense one detected at 376 nm ($^4I_{15/2} \rightarrow {}^4G_{11/2}$ transition) and another higher energy one located at 363 nm ($^4I_{15/2} \rightarrow {}^4G_{9/2}$ transition) are considered in registering all S1–S6 glasses' luminescence spectra. Figs. 3 (b) and (c) display the recorded luminescence spectra under 363 nm and 376 nm pumpings for all S1–S6 samples at 400–700 nm spectral range respectively. All glasses exhibit an asymmetric wide emission band centered at 550 nm (18,181 cm^{-1}) owing to $^4S_{3/2} \rightarrow {}^4I_{15/2}$ transition [65] where sample S1 additionally shows a band peaked at 454 nm (22,026 cm^{-1}) corresponding to the transition $^4F_{5/2} \rightarrow {}^4I_{15/2}$ upon $\lambda_{exci.}$ = 363 nm. Here following their excitation intensities at 363 nm and 376 nm, samples S1 and S6 accordingly exhibit higher fluorescence intensities in all glasses for the 550 nm fluorescence band (see Figs. 3 (a), (b),

and (c)). Interestingly at 400–500 nm range, a broad emission band is also observed for all samples under $\lambda_{exci.} = 376$ nm and except for sample S1 at $\lambda_{exci.} = 363$ nm. Though the transitions from Er^{3+}: $^2G_{9/2}$ and $^4F_{3/2}$, $^4F_{5/2}$, $^4F_{7/2}$ levels to $^4I_{15/2}$ state represent violet and blue emissions [64], in our case, the broad luminescence appeared at 400–500 nm span might be due to the defects present in the host matrix. To test this assumption, we recorded excitation spectra at $\lambda_{emi.} = 450$ nm (into the broad emission band at 400–500 nm span) and $\lambda_{emi.} = 550$ nm (into the Er^{3+}: $^4S_{3/2} \rightarrow {}^4I_{15/2}$ emission) for glass S2 as an example (see Fig. 3 (d)). Here the excitation spectrum obtained at 450 nm shows some bands that could be linked to host defects. In fact, such a broad band is noticed in the emission spectrum of the host glass excited at 290 nm (see Fig. 3 (e)). So, such a wide emission band between 400 and 500 nm observed in the luminescence spectra of studied samples could be associated with host defects.

3.7. Radiative parameters

For all S1–S6 samples, utilizing Ω_2, Ω_4, and Ω_6 values and refractive indices, radiative traits like A_{ed}, A_{md}, A_R, β_R, and τ_{rad} for all possible optical transitions of Er^{3+}: $^4F_{5/2}$, $^4F_{7/2}$, $^2H_{11/2}$, $^4S_{3/2}$, $^4F_{9/2}$, $^4I_{9/2}$, $^4I_{11/2}$, and $^4I_{13/2}$ excited levels are computed employing relevant formulae [71,72]. Obtained such results for sample S1 are provided in Table 6 and for the rest of S2–S6 glasses in Table S2 (i-v) in SM separately. In all glasses, sample S1 has comparably a larger A_R (= 206 s^{-1}) for transition $^4I_{13/2} \rightarrow {}^4I_{15/2}$ indicating its better potential for ~1.53 μm optical amplification. S1–S6 glasses all show β_R = 100% for $^4I_{13/}$

Table 6 – Emission transitions (SLJ → S′L′J′), energy (υ, cm^{-1}), wavelength (λ_{em}, nm), electric (A_{ed}, $\times 10^{-20}$ cm^2) and magnetic (A_{md}, $\times 10^{-20}$, cm^2) dipole line strengths, total radiative (A_R, s^{-1}) transition probability, calculated (β_R) branching ratios, and radiative (τ_{rad}, μs) lifetimes for various excited states of the Er^{3+} ion in S1 glass. The experimental lifetime (τ_{exp}, μs) of $^4S_{3/2}$ level with its corresponding quantum yield (η, %) and experimental branching ratio (β_{exp}) to the ground state ($^4I_{15/2}$) are also included.

Transitions	Energy	λ_{em}	A_{ed}	A_{md}	A_R	β_R	τ_{rad}
$^4F_{5/2} \rightarrow {}^4F_{7/2}$	1236	8088	1	0	1	0.00	252.30
$\rightarrow {}^2H_{11/2}$	3845	2601	11	–	11	0.00	
$\rightarrow {}^4S_{3/2}$	3878	2579	1	–	1	0.00	
$\rightarrow {}^4F_{9/2}$	6783	1474	149	–	149	0.04	
$\rightarrow {}^4I_{9/2}$	9495	1053	129	–	129	0.04	
$\rightarrow {}^4I_{11/2}$	11,822	846	123	–	123	0.03	
$\rightarrow {}^4I_{13/2}$	15,495	645	1555	–	1555	0.39	
$\rightarrow {}^4I_{15/2}$	22,026	454	1993	–	1993	0.50	
$^4F_{7/2} \rightarrow {}^2H_{11/2}$	2608	3834	8	–	8	0.00	188.49
$\rightarrow {}^4S_{3/2}$	2641	3786	0	–	0	0.00	
$\rightarrow {}^4F_{9/2}$	5546	1803	8	–	8	0.00	
$\rightarrow {}^4I_{9/2}$	8259	1211	196	–	196	0.04	
$\rightarrow {}^4I_{11/2}$	10,586	945	293	–	293	0.06	
$\rightarrow {}^4I_{13/2}$	14,258	701	541	–	541	0.10	
$\rightarrow {}^4I_{15/2}$	20,790	481	4258	–	4258	0.80	
$^2H_{11/2} \rightarrow {}^4S_{3/2}$	33	303,050	0	–	0	0.00	164.62
$\rightarrow {}^4F_{9/2}$	2938	3404	10	–	10	0.00	
$\rightarrow {}^4I_{9/2}$	5650	1770	67	–	67	0.01	
$\rightarrow {}^4I_{11/2}$	7978	1253	54	–	54	0.01	
$\rightarrow {}^4I_{13/2}$	11,650	858	110	–	110	0.02	
$\rightarrow {}^4I_{15/2}$	18,182	550	5833	–	5833	0.96	
$^4S_{3/2} \rightarrow {}^4F_{9/2}$	2905	3442	1	–	1	0.00	406.86
$\rightarrow {}^4I_{9/2}$	5617	1780	72	–	72	0.03	
$\rightarrow {}^4I_{11/2}$	7945	1259	49	–	49	0.02	
$\rightarrow {}^4I_{13/2}$	11,617	861	680	–	680	0.28	
$\rightarrow {}^4I_{15/2}$	18,149	551	1656	–	1656	0.67	
$^4S_{3/2} \rightarrow {}^4I_{15/2}$							
β_{exp}	0.27	τ_{exp}	9.75	η	2.40		
$^4F_{9/2} \rightarrow {}^4I_{9/2}$	2713	3687	4	–	4	0.00	560.88
$\rightarrow {}^4I_{11/2}$	5040	1984	95	–	95	0.06	
$\rightarrow {}^4I_{13/2}$	8712	1148	77	–	77	0.04	
$\rightarrow {}^4I_{15/2}$	15,244	656	1607	–	1607	0.90	
$^4I_{9/2} \rightarrow {}^4I_{11/2}$	2327	4297	1	3	4	0.02	4104.79
$\rightarrow {}^4I_{13/2}$	6000	1667	79		79	0.32	
$\rightarrow {}^4I_{15/2}$	12,531	798	161		161	0.66	
$^4I_{11/2} \rightarrow {}^4I_{13/2}$	3672	2723	27	13	40	0.16	4020.80
$\rightarrow {}^4I_{15/2}$	10,204	980	208		208	0.84	
$^4I_{13/2} \rightarrow {}^4I_{15/2}$	6532	1531	159	47	206	1.00	4863.59

$_2 \rightarrow {}^4I_{15/2}$ transition, and sample S3 owns the highest τ_{rad} (= 5.92 ms) where generally longer τ_{rad} is necessary to reduce laser threshold. Also, for MIR laser transition ($^4I_{11/2} \rightarrow {}^4I_{13/2}$), glass S3 retains a longer τ_{rad} (= 4.972 ms) in all S1–S6 samples. For $^4S_{3/2}$ upper-state calculated τ_{rad} value is 406.86 μs, 491.91 μs, 540.69 μs, 424.53 μs, 499.10 μs, and 486.53 μs accordingly in S1, S2, S3, S4, S5, and S6 glasses. Here, β_{exp} quantities are computed taking into account relative areas under the fluorescence bands.

3.8. CIE (x,y) coordinates and CP

For all S1–S6 samples, to understand gross visible emissions at $\lambda_{exci.}$ = 363 nm and $\lambda_{exci.}$ = 376 nm, related CIE 1931 (x, y) values are computed from Figs. 3 (b) and (c) utilizing $\bar{x}(\lambda)$, $\bar{y}(\lambda)$, and $\bar{z}(\lambda)$ color functions where spectral power intensity (P(λ)) could be represented as [44]:

$$X = \int \bar{x}(\lambda)P(\lambda)d\lambda \quad (7)$$

$$Y = \int \bar{y}(\lambda)P(\lambda)d\lambda \quad (8)$$

and

$$Z = \int \bar{z}(\lambda)P(\lambda)d\lambda \quad (9)$$

where X, Y, and Z = tristimulus values, x = X/X + Y + Z, y = Y/X + Y + Z.

Obtained (x, y) values are listed in Table 7. Figs. 4 (a) and (b) exhibit relevant 2-D CIE chromaticity plots for all S1–S6 glasses upon $\lambda_{exci.}$ = 363 nm and $\lambda_{exci.}$ = 376 nm accordingly. All S1–S6 samples emit an overall color of purplish-blue to blue and blue to greenish-blue to green under respective $\lambda_{exci.}$ = 363 nm and $\lambda_{exci.}$ = 376 nm (see Table 7) where commercial blue phosphor BAM ($BaMgAl_{10}O_{17}:Eu^{2+}$) color coordinates are (0.142, 0.107). Here emitted color from a glass could be altered by changing pumping wavelength.

Further, by using CIE coordinates, for all S1–S6 glasses CP (%) values are evaluated by employing the formula [44] as:

$$CP = \sqrt{\frac{(x - x_i)^2 + (y - y_i)^2}{(x_d - x_i)^2 + (y_d - y_i)^2}} \times 100\ \% \quad (10)$$

where (x_d, y_d) = dominant wavelength coordinates, (x, y) = sample point coordinates, and (x_i, y_i) = (0.310, 0.316) = CIE1931 Standard Source I illuminate point coordinates.

Under $\lambda_{exci.}$ = 363 nm derived (x_d, y_d) for all S1–S6 samples are (0.1273, 0.0547), (0.1304, 0.0471), (0.1126, 0.0817), (0.1086,

Table 7 – Excitation wavelength ($\lambda_{exci.}$), CIE 1931 color coordinates, dominant emission wavelength (λ_d), color purity (CP), and emission color for all the studied S1–S6 glasses.

Glass code	$\lambda_{exci.}$ (nm)	CIE1931 (x, y)	λ_d (nm)	CP (%)	Emission color
S1	363	(0.1731, 0.1190)	468	75.3	purplish-blue
S2	363	(0.1703, 0.1087)	467	77.3	purplish-blue
S3	363	(0.1925, 0.1743)	473	60.1	blue
S4	363	(0.1870, 0.1711)	475	61.5	blue
S5	363	(0.1644, 0.0973)	467	80.7	purplish-blue
S6	363	(0.1888, 0.1800)	475	60.1	blue
S1	376	(0.2463, 0.4216)	513	22.4	green
S2	376	(0.1989, 0.2334)	481	49.1	blue
S3	376	(0.2102, 0.2566)	483	42.7	greenish-blue
S4	376	(0.2040, 0.2612)	484	43.9	greenish-blue
S5	376	(0.1793, 0.1683)	475	65.2	blue
S6	376	(0.2290, 0.3797)	501	26.7	green

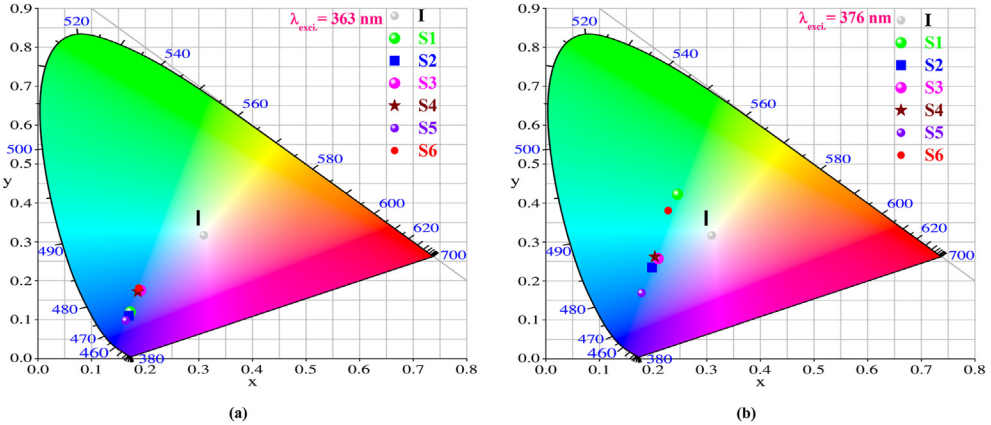

Fig. 4 – 1931 CIE color chromaticity coordinates diagram for all the 1.0 mol% Er^{3+}-doped single and mixed alkali oxides containing glasses under (a) 363 nm and (b) 376 nm excitation wavelengths.

0.0817), (0.1297, 0.0448), and (0.1071, 0.0908) individually while the same coordinates upon $\lambda_{exci.}$ = 376 nm for such glasses are (0.0238, 0.7871), (0.0861, 0.1447), (0.0747, 0.1793), (0.0670, 0.1931), (0.1071, 0.0918), and (0.0044, 0.5525) accordingly. Calculated CP values are given in Table 7. Upon $\lambda_{exci.}$ = 363 nm, S1, S2, and S5 glasses could produce emission purplish-blue of 467–468 nm as λ_d (dominant wavelength) with CP > 75%. Under $\lambda_{exci.}$ = 376 nm, sample S5 is capable to generate an emission blue of 475 nm as λ_d with CP > 65%. Therefore the capability of the studied samples to emit purplish-blue or blue light under 363 or 376 nm excitation make them potentially suitable for application in W-LEDs.

3.9. Visible emissin deday analysis

For all S1–S6 glasses, Fig. 5 (a) illustrates recorded Er^{3+}: $^4S_{3/2}$ upper-level decay time patterns under $\lambda_{exci.}$ = 376 nm for 550 nm fluorescence band. Here $^4S_{3/2}$ level decay profiles of all S1–S6 glasses exhibit a non-exponential nature. Normally, if excitation energy directly transfers from an excited Er^{3+} ion to a non-excited Er^{3+} ion, for the decay curves a non-exponential trend appears. To find out decay time values, each curve is well fitted to double exponential functions with R-squared (R^2) value at 0.99388–0.99924 span using the following expression [44]:

$$y = y_0 + A_1 \exp\left(\frac{-x}{\tau_1}\right) + A_2 \exp\left(\frac{-x}{\tau_2}\right) \quad (11)$$

where τ_1 and τ_2 = rapid and slow decay time components, y = emission intensity, y_0 = constant, x = time, A_1 and A_2 = fitting constants or exponential pre-factors.

Later average lifetime (τ) is computed as [44]:

$$\tau = \frac{A_1\tau_1^2 + A_2\tau_2^2}{A_1\tau_1 + A_2\tau_2} \quad (12)$$

Figs. 5 (b-g) presents decay time profiles fit of Er^{3+}: $^4S_{3/2} \rightarrow {}^4I_{15/2}$ transition for all S1–S6 samples.

9.75 μs, 11.29 μs, 10.59 μs, 9.37 μs, 10.69 μs, and 11.24 μs respectively are the derived lifetimes (τ_{meas}) for S1, S2, S3, S4, S5, and S6 glasses for $^4S_{3/2}$ state. Here glass S2 has relatively greater τ_{meas} in all glasses for $^4S_{3/2} \rightarrow {}^4I_{15/2}$ transition, hinting at lesser CR (cross-relaxation) processes among Er^{3+} ions in it. As it is known, in Er^{3+} ion $^2H_{11/2}$ and $^4S_{3/2}$ levels are very close to each other (ΔE (energy gap) ~780 cm^{-1}) and excited ions' relaxation in such two levels includes three distinct channels such as (a) radiative transitions (b) multiphonon transitions and (c) CR. 'η' for Er^{3+}: $^4S_{3/2}$ level in all samples is calculated ($\eta = \frac{\tau_{meas}}{\tau_{rad}} \times 100$ %) and given in Table 6 and Table S2 (i-v) accordingly.

3.10. NIR luminescence

Within the 1400–1650 nm wavelength range, Fig. 6 (a) shows registered NIR fluorescence spectra of all S1–S6 samples under 980 nm LD excitation operated at 50 mW output. A typical wide asymmetric emission band peaked at 1532 nm (6527 cm^{-1}) assigned to Er^{3+}: $^4I_{13/2} \rightarrow {}^4I_{15/2}$ transition [65] is identified for all glasses, and its intensity exhibits reliance on added single or mixed alkali oxides. In all samples, Li–Na mixed ions comprising one (S4 glass) has comparably higher intensity. Here obtained NIR emission (constitutes both MD and ED contributions) covers the entire C- + L- (1.565–1.625 μm) optical bands' region suggesting such glasses' potential application in optical amplifiers. Generally, owing to the $^4I_{15/2}$ state's Stark splitting, the NIR luminescence band ($^4I_{13/2} \rightarrow {}^4I_{15/2}$) splits into distinct bands [25]. In all samples, observed broad NIR luminescence consists of five Gaussian bands centered at 1494 nm, 1532 nm, 1540 nm, 1556 nm, and 1605 nm accordingly. As an example, Fig. 6 (b) shows the deconvoluted NIR emission spectrum for sample S4 at 1400–1650 nm range. Here narrow 1532 nm, 1540 nm, and 1556 nm bands represent MD, and broad 1494 nm and 1605 nm peaked bands represent ED elements.

3.11. NIR luminescence decay analysis

Figs. 7 (a-f) display Er^{3+}: $^4I_{13/2} \rightarrow {}^4I_{15/2}$ fluorescence transition decay curves for all S1–S6 glasses recorded under 980 nm LD pumping. As can be seen from Figs. 7 (a-f), $^4I_{13/2}$ level decay profiles could be well fit to single-exponential functions (R^2 = 0.99959–0.99976 range) [9] as:

$$I(t) = y_0 + A \exp\left(\frac{-t}{\tau}\right) \quad (13)$$

where A = constant, I(t) = fluorescence intensity, and 'τ' = luminescence decay time.

Obtained decay times (τ_{meas}) of $^4I_{13/2}$ metastable state are given in Table 8. In all samples, glass S5 possesses a relatively longer decay time (4.34 ms). Usually, longer decay times of $^41_{13/2}$ level provide required large population inversion under adopted reasonable pump powers for optical amplification. In comparison, τ_{meas} value for glass S5 is found to be lower than those of $50TeO_2$–$39ZnF_2$–$9ZnO$–$1ZnS$–$1ErF_3$ (mol%) (= 6.08 ms) [16], PAN1Er5LiF-CA (= 7.74 ms) [33], and 1Er ZMB (= 4.686 ms) [65] glasses' respective value and higher than those of $25Li_2O$–$15Bi_2O_3$–$44B_2O_3$–$15TeO_2$–$1Er_2O_3$ (mol%) (= 0.556 ms) [35], NPbPEr-1.0 (= 4.20 ms) [67], Er^{3+}: Phosphate (= 2.8 ms) [74], Er^{3+}: Fluorotellurite (= 3.06 ms) [75], and SANSCEr10 (= 3.83 ms) [76] glasses' corresponding value. So, for C-band optical amplification, owing to the longer τ_{meas} of Er^{3+}: $^4I_{13/2}$ level in it, glass S5 could be favorable for achieving higher population inversion than such compared glasses reported in Refs. [35, 67, 74–76]. Anyhow, acquired τ_{meas} values of all S1–S6 samples are lesser than that of Er^{3+}: Silicate L-22 glass (= 14.5 ms) [26] standard value, as here studied samples not optimized in composition for obtaining larger τ_{meas} values of Er^{3+}: $^4I_{13/2} \rightarrow {}^4I_{15/2}$ transition, which is our another task for future.

Further, using 'τ_{rad}' and 'τ_{meas}' values, calculated 'η' values of Er^{3+}: $^4I_{13/2}$ level in all S1–S6 glasses are listed in Table 8. Here, sample S4 owns the highest η (82%) in all glasses.

Owing to MPR processes η < 100% *i.e.*, $\tau_{meas} < \tau_{rad}$. For $^4I_{13/2}$ level, W_{NR} (MPR rate) could be obtained [65] as:

$$W_{NR} = \frac{1}{\tau_{meas}} - \frac{1}{\tau_{rad}} \quad (14)$$

Derived W_{NR} for $^4I_{13/2}$ level in individual S1, S2, S3, S4, S5, and S6 samples is 71.9 s^{-1}, 60.6 s^{-1}, 66.9 s^{-1}, 42.5 s^{-1}, 52.8 s^{-1}, and 67.9 s^{-1}. Such W_{NR} could arise due to S1–S6 glasses' larger

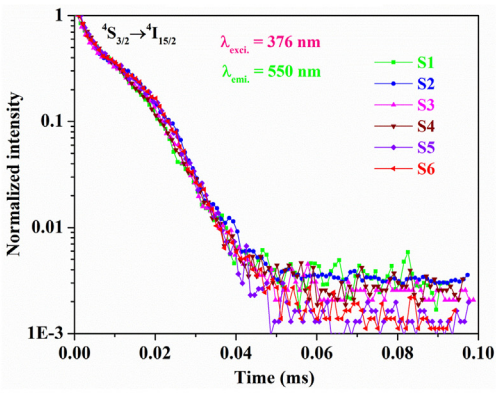

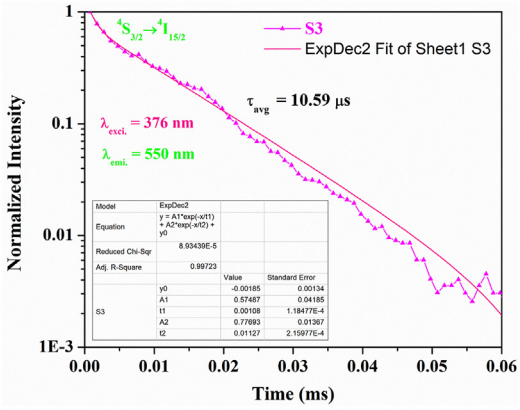

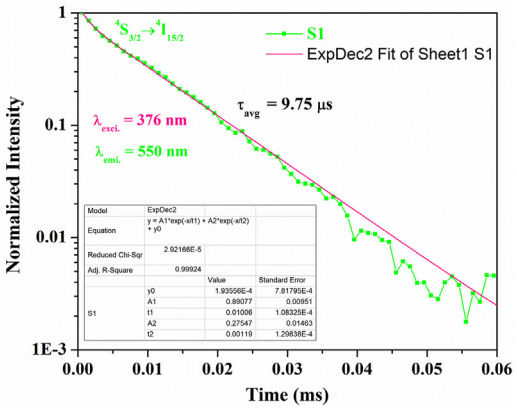

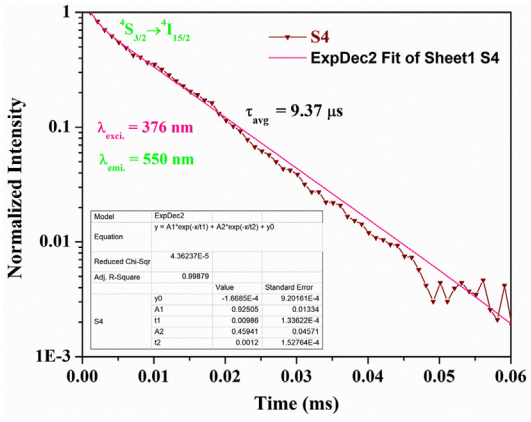

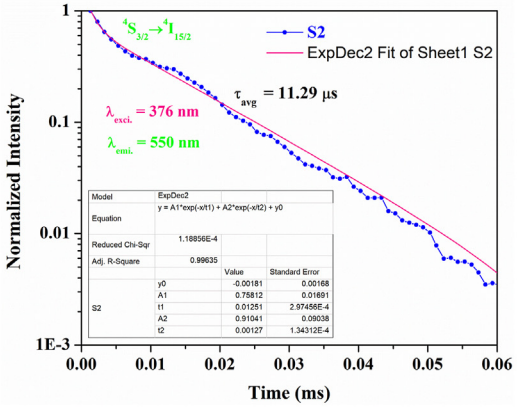

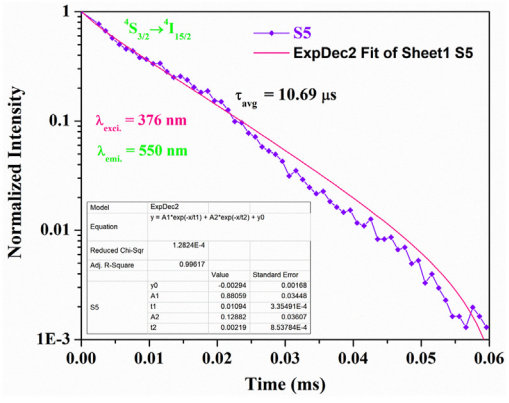

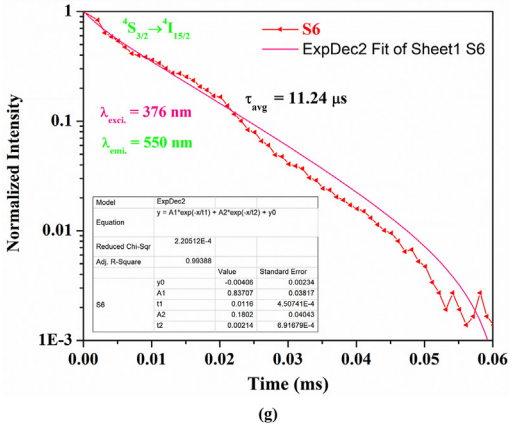

Fig. 5 – (a) Decay lifetime profiles of the Er^{3+}: $^4S_{3/2} \rightarrow {}^4I_{15/2}$ transition for all S1–S6 glasses under 376 nm excitation wavelength (b–g) Decay lifetime profiles fit of the Er^{3+}: $^4S_{3/2} \rightarrow {}^4I_{15/2}$ transition for all S1–S6 glasses.

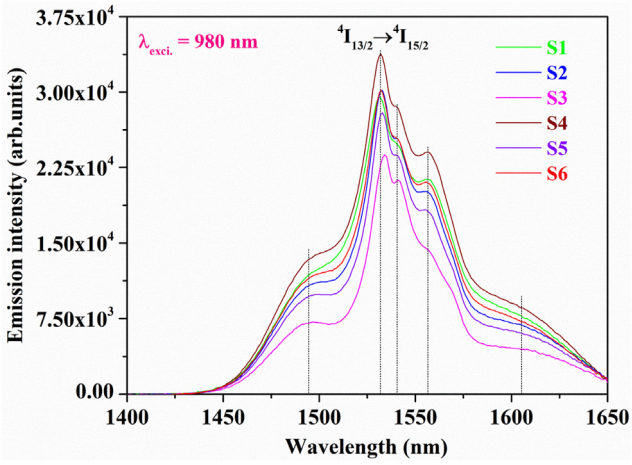

Fig. 6 – (a) NIR luminescence spectra of all the 1.0 mol% Er^{3+}-doped glasses upon 980 nm LD excitation. (b) Deconvoluted NIR emission spectrum of glass S4.

phonon energy and ET (energy transfer) from Er^{3+} to hydroxyl (OH^-) groups. Greater η and low W_{NR} are crucial for high-gain amplifiers and lasers.

3.12. *NIR optical amplifier parameters*

Later, for all S1–S6 glasses, to inspect identified NIR fluorescence qualitatively, by scaling Fig. 6 σ_{emi} (stimulated emission cross-section) is evaluated applying the Füchtbauer–Ladenburg formula [77] as:

$$\sigma_{emi}(\lambda) = \frac{A_{ij}}{8\pi c n^2} \times \frac{\lambda^5 I(\lambda)}{\int \lambda I(\lambda) d\lambda} \quad (15)$$

where c, n, A_{ij} (= A_{ed} + A_{md}), and $I(\lambda)$ denote light speed in vacuum, refractive index, spontaneous fluorescence probability, and fluorescence relative intensity at λ from i to j state correspondingly.

Fig. 8 (a) shows obtained σ_{emi} patterns of all S1–S6 samples for $^4I_{13/2} \rightarrow {}^4I_{15/2}$ transition at 1400–1650 nm span and from such plots derived peak σ_{emi} (σ_{max}^{emi}) quantities are given in Table 8.

In this case, $\Delta\lambda_{eff}$ (effective bandwidth) for NIR luminescence band is calculated *via* the relation [9]:

$$\Delta\lambda_{eff} = \frac{1}{I_{max}} \int I(\lambda) d\lambda \quad (16)$$

where I_{max} = intensity at band maximum.

Evaluated $\Delta\lambda_{eff}$ values for all S1–S6 samples are listed in Table 8. Further, $\sigma_{max}^{emi} \times \Delta\lambda_{eff}$ (peak gain bandwidth) and $\sigma_{max}^{emi} \times \tau_{rad}$ (optical gain) are calculated and given in Table 8 along with A_{ed}, A_{md}, A_R, β_R, β_{exp}, and τ_{rad} for $^4I_{13/2} \rightarrow {}^4I_{15/2}$ transition.

For designing optimized fiber lasers and optical amplifiers, higher σ_{emi} for Er^{3+}: $^4I_{13/2} \rightarrow {}^4I_{15/2}$ transition is necessary. Also, larger $\Delta\lambda_{eff}$ is essential in enhancing the WDM systems' capacity. Here $\Delta\lambda_{eff}$ primarily relies on NIR emission's inhomogeneous broadening owing to disorderness in glass network structure. From sample S1 to S3 reduction in $\Delta\lambda_{eff}$ specifies that with changing alkali ions, Er^{3+} ions' ligand field alters with site-to-site changes [78]. Here $\sigma_{emi} \times \Delta\lambda_{eff}$ and $\sigma_{emi} \times \tau_{rad}$ products reveal the amplification and laser threshold of studied samples. In all S1–S6 glasses, sample S1 holds relatively greater $\Delta\lambda_{eff}$ and $\sigma_{max}^{emi} \times \Delta\lambda_{eff}$ for $^4I_{13/2} \rightarrow {}^4I_{15/2}$ transition, indicating its potential for broadband amplification. Comparably, $\Delta\lambda_{eff}$ of $^4I_{13/2} \rightarrow {}^4I_{15/2}$ transition in glass S1 is larger than those of PANK1Er5LiF-AC (= 43.5 nm) [33], TG01 (= 71 nm) [75], SANSCEr10 (= 53 nm) [76], Er^{3+}: ZBLAN (= 65 nm) [78], and Er^{3+}: GGL (= 54.5 nm) [79] glasses' related values and lower than those of S1 (= 90 nm) [16], $98TeO_2–2Er_2O_3$ (= 93.2 nm) [29], and LBBTE1 (= 99.31 nm) [35] glasses' individual values. Likewise, $\sigma_{max}^{emi} \times \Delta\lambda_{eff}$ value of $^4I_{13/2} \rightarrow {}^4I_{15/2}$ in sample S1 is greater than those of $50TeO_2–39ZnF_2–9ZnO–1ZnS–1ErF_3$ (= 4.176×10^{-26} cm^3) [16], 1Er ZMB (= 3.944×10^{-26} cm^3) [65], LiBEr5 (= 4.1525×10^{-26} cm^3) [66], SANSCEr10 (= 5.194×10^{-26} cm^3) [76], Er^{3+}: ZBLAN (= 3.315×10^{-26} cm^3) [78], and Er^{3+}: GGL (= 4.24×10^{-26} cm^3) [79] glasses' corresponding values and lower than those of LBBTE1 (= 8.29×10^{-26} cm^3) [35] and TG1 (= 6.048×10^{-26} cm^3) [75] glasses' respective values.

Later, taking into account β_R and σ_{emi}, with anticipation that $^4I_{13/2}$ state is populated by Er^{3+} ions at 20–100% range under 980 nm excitation, for all S1–S6 samples, for NIR fluorescence theoretical gain is estimated utilizing an expression [80]:

$$G(\lambda, P) = 10 \log_{10} \exp(PN\beta_R \sigma_{emi}(\lambda)) \quad (17)$$

where P = excited Er^{3+} ions' fractional factor in $^4I_{13/2}$ level, N = total Er^{3+} ion concentration.

Fig. 8 (b) exhibits calculated theoretical gain spectra of $^4I_{13/2} \rightarrow {}^4I_{15/2}$ transition at 1400–1650 nm span for S1 glass. For the rest of the S2–S6 samples the attained similar spectra are shown inFigs. S2 (a-e) in SM separately. Here, sample S1 shows a relatively higher $G(\lambda, P)$ (= 7.951 dB/cm) while S6 glass has the minimal $G(\lambda, P)$ (= 6.644 dB/cm) value at 1532 nm in all samples for P = 100%. Also, $G(\lambda, P)$ reduces in S1>S2>S3 and S4>S5>S6 order with changing single or mixed alkali ions. At P = 60%, S1 glass possesses a $G(\lambda, P)$ value of 4.771 dB/cm.

3.12.1. *McCumber's theory*

Further, σ_{abs} (absorption cross-section) of $^4I_{15/2} \rightarrow {}^4I_{13/2}$ transition could be evaluated from Fig. 2 (a) using equation [81]:

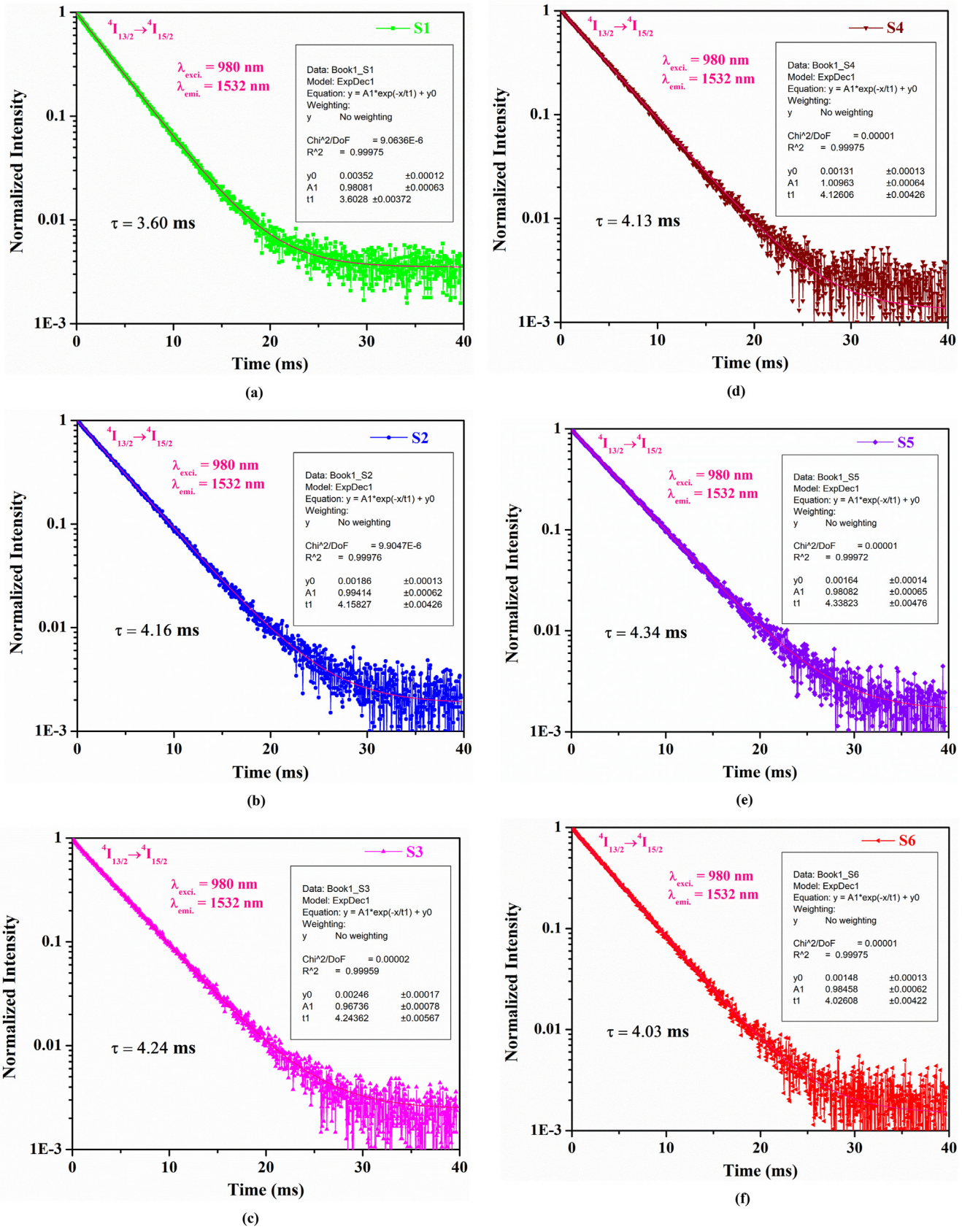

Fig. 7 – (a–f) Decay lifetime profiles of the Er^{3+}: $^4I_{13/2} \rightarrow {}^4I_{15/2}$ transition for all S1–S6 glasses under 980 nm excitation wavelength.

Table 8 – Wavelength (λ, nm), electric (A_{ed}, s^{-1}), magnetic (A_{md}, s^{-1}) and total radiative transition probabilities (A_R, s^{-1}), branching ratios (β_R, β_{exp} %), radiative (τ_{rad}, ms) and measured (τ_{meas}, ms) lifetimes, quantum efficiency (η, %), effective bandwidth ($\Delta\lambda_{eff}$, nm), stimulated peak emission cross-section (σ^{emi}_{max}, × 10^{-21} cm^2), gain bandwidth ($\sigma^{emi}_{max} \times \Delta\lambda_{eff}$, × 10^{-26} cm^3), and optical gain ($\sigma^{emi}_{max} \times \tau_{rad} \times 10^{-23}$ $cm^2 s$) of the $^4I_{13/2} \rightarrow {}^4I_{15/2}$ emission transition for all the S1–S6 glasses.

Sample Code	λ	A_{ed}	A_{md}	A_R	β_R, β_{exp}	τ_{rad}	τ_{meas}	η	$\Delta\lambda_{eff}$	σ^{emi}_{max}	$\sigma^{emi}_{max} \times \Delta\lambda_{eff}$	$\sigma^{emi}_{max} \times \tau_{rad}$
S1	1531	159	47	206	100, 73	4.86	3.60	74	74.660	7.212	5.384	3.505
S2	1532	132	48	180	100, 82	5.56	4.16	75	66.663	7.018	4.678	3.902
S3	1532	120	49	169	100, 80	5.92	4.24	72	59.816	7.249	4.336	4.291
S4	1532	152	48	200	100, 79	5.01	4.13	82	72.503	7.137	5.175	3.575
S5	1532	129	49	178	100, 82	5.63	4.34	77	64.208	7.142	4.586	4.021
S6	1532	131	49	180	100, 71	5.55	4.03	73	70.343	6.584	4.631	3.654

$$\sigma_{abs}(\lambda) = \frac{2.303}{tN_{Er^{3+}}} O.D.(\lambda) \quad (18)$$

where *O.D.* (λ) = optical density at wavelength λ, $N_{Er^{3+}}$ = Er^{3+} ions' concentration in glass, t = sample thickness.

Next, σ_{abs} and σ_{emi} could be related by McCumber's theory [82] as:

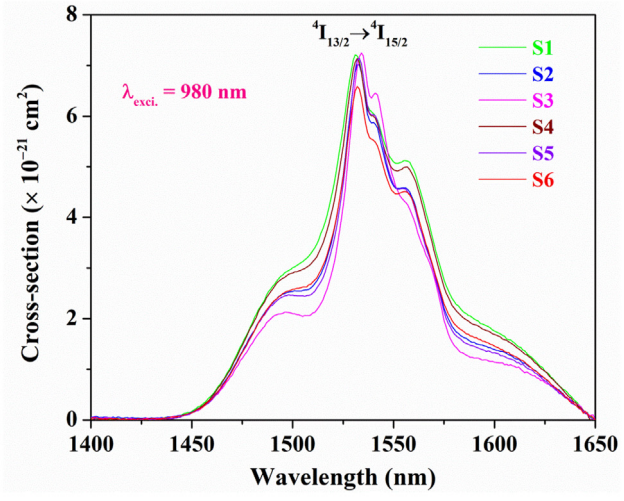

Fig. 8 – (a) Stimulated emission cross–section profiles of the Er^{3+}: $^4I_{13/2} \rightarrow {}^4I_{15/2}$ transition for all S1–S6 glasses (b) Predicted theoretical gain spectra of the $^4I_{13/2} \rightarrow {}^4I_{15/2}$ transition for glass S1.

$$\sigma_{abs}\left(\lambda\right) = \sigma_{emi}\left(\lambda\right) \times \left(\frac{Z_u}{Z_l}\right) \exp\left[\frac{-\left(E_{zl} - hc\lambda^{-1}\right)}{K_B T}\right] \quad (19)$$

where T = temperature, h = Planck's constant, Ezl = energy gap between the lowest Stark level of upper ($^4I_{13/2}$) and lower ($^4I_{15/2}$) states at T = 300 K, K_B = Boltzmann constant, and Z_u and Z_l = upper and lower manifolds' partition functions.

Following Eqs. (18) and (19), calculated σ_{abs} and σ^M_{emi} profiles for sample S1 at 1400–1700 nm range are illustrated in Fig. 9 (a) and for remaining all S2–S6 glasses derived similar plots are presented in Figs. S3 (a-e) in SM individually. Table 9 presents peak σ_{abs} ($^4I_{15/2} \rightarrow {}^4I_{13/2}$) and σ^M_{emi} ($^4I_{13/2} \rightarrow {}^4I_{15/2}$) values in all S1–S6 samples. In all S1–S6 samples, peak σ_{abs} value of $^4I_{15/2} \rightarrow {}^4I_{13/2}$ varied at 1.260–1.459 × 10^{-20} with changing single or mixed alkali ions. In all glasses, sample S1 ('Li' ions added one) shows the highest peak σ_{abs} and σ^M_{emi} values.

In comparison, σ^M_{emi} value of $^4I_{13/2} \rightarrow {}^4I_{15/2}$ transition in glass S1 is higher than those of $50TeO_2$–$39ZnF_2$–9ZnO–1ZnS–$1ErF_3$ (= 0.464 × 10^{-20} cm^2) [16], LBBTE1 (= 0.8348 × 10^{-20} cm^2) [35], 1Er ZMB (= 0.457 × 10^{-20} cm^2) [65], LiBEr5 (= 0.396 × 10^{-20} cm^2) [66], NPbPEr-0.5 (= 0.74872 × 10^{-20} cm^2) [67], TG1 (= 0.84 × 10^{-20} cm^2) [75], SANSCEr10 (= 0.488 × 10^{-20} cm^2) [76], $80TeO_2$-9.5ZnO-$9.5Na_2O$–$1Er_2O_3$ (= 0.85 × 10^{-20} cm^2) [78], Er^{3+}: Fluoroaluminate (= 0.53 × 10^{-20} cm^2) [81], and BLK1.0Er (= 1.1072 × 10^{-20} cm^2) [83] glasses' respective values and lower than that of LiPbAlB1.5Er (= 2.34 × 10^{-20} cm^2) [34] glass related value.

Additionally, *G*(λ, *P*) (Gain cross-section) could be estimated from derived σ_{abs} and σ^M_{emi} by following relation [81]:

$$G(\lambda, P) = [P \times \sigma_{emi}(\lambda) - (1 - P) \times \sigma_{abs}(\lambda)] \quad (20)$$

where P = population inversion (0–1). Here P value represents the population on the $^4I_{13/2}$ level to the total population at the $^4I_{13/2}$+$^4I_{15/2}$ levels' ratio.

G(λ, *P*) profile of $^4I_{13/2} \rightarrow {}^4I_{15/2}$ transition in glass S1 at 1400–1700 nm range is depicted in Fig. 9 (b) and for the rest of the S2–S6 samples such spectra are depicted in Figs. S4 (a-e) in SM accordingly. In Fig. 9 (b), dotted lines signify S- (1.46–1.53 μm), C- (1.53–1.565 μm), and L-(1.565–1.625 μm) optical bands amplification region. As can be seen from Fig. 9 (b) amplification in the C-optical band starts when P = 50%. Obtained maximum value at P = 1 is found to be 1.692 × 10^{-20} cm^2 for S1 glass. Evaluated gain cross-section varied at 1.459–1.692 × 10^{-20} cm^2 range at 1.532 μm for all studied glasses. Considering higher σ^M_{emi}, σ_{abs}, $\Delta\lambda_{eff}$, $\sigma^{emi}_{max} \times \Delta\lambda_{eff}$, and moderate τ_{meas} values of $^4I_{13/2} \rightarrow {}^4I_{15/2}$ transition in sample S1, it could be favorable for broadband amplification. Honestly, here we presented the Gain values

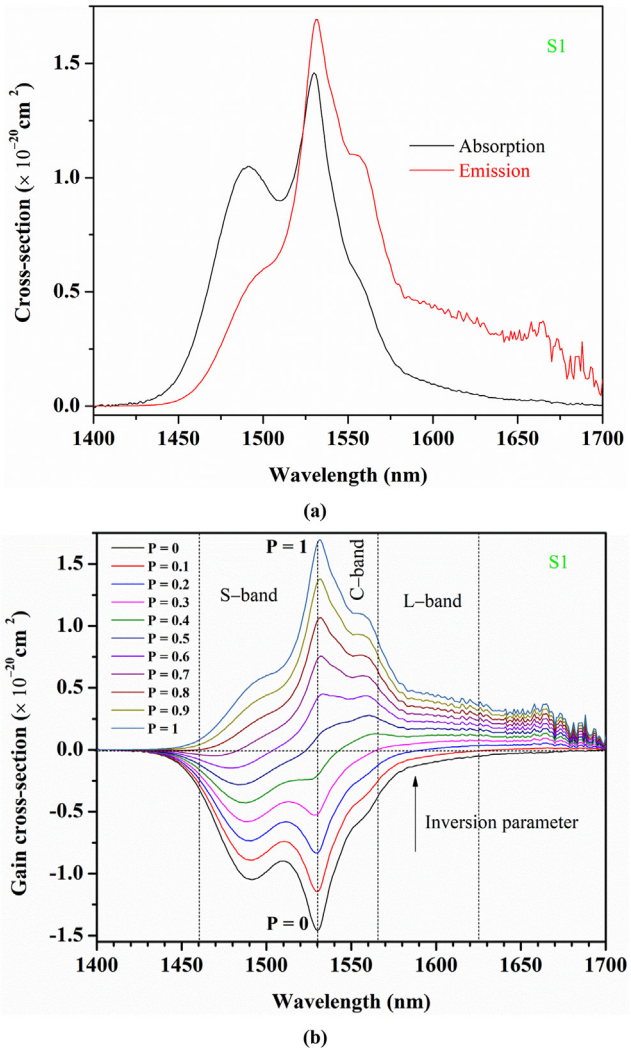

Fig. 9 – (a) Absorption cross-section ($^4I_{15/2} \rightarrow {}^4I_{13/2}$ transition) and stimulated emission cross-section ($^4I_{13/2} \rightarrow {}^4I_{15/2}$ transition) profiles of S1 glass (b) Calculated gain spectra of $^4I_{13/2} \rightarrow {}^4I_{15/2}$ transition at different P values for sample S1. Here, dotted lines indicate S-, C-, and L-optical bands amplification region.

Table 9 – Values of peak absorption cross-section (σ_{abs}) of $^4I_{15/2} \rightarrow {}^4I_{13/2}$ transition and emission cross-section (σ^M_{emi}) (from Mc-Cumber theory) of $^4I_{13/2} \rightarrow {}^4I_{15/2}$ transition in all S1–S6 glasses.

Sample Code	σ_{abs} (× 10^{-20} cm^2)	σ^M_{emi} (× 10^{-20} cm^2)
S1	1.459	1.692
S2	1.268	1.459
S3	1.272	1.504
S4	1.400	1.649
S5	1.281	1.483
S6	1.260	1.462

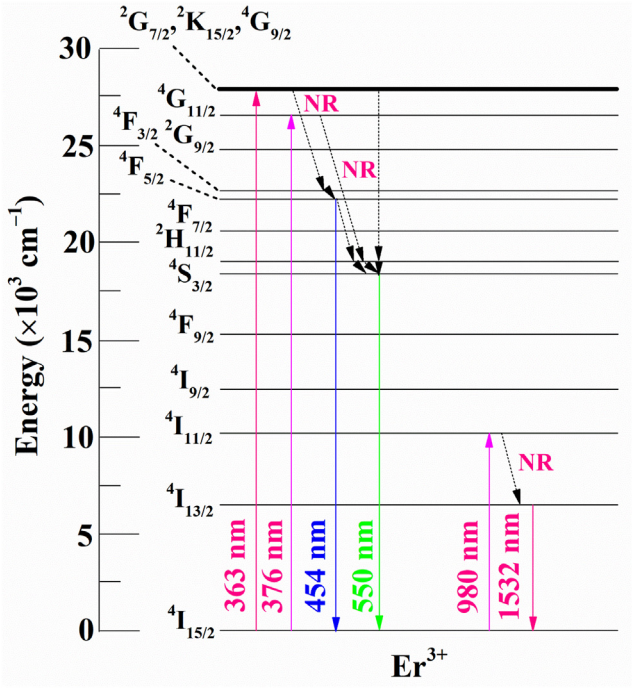

Fig. 10 – Partial energy-level diagram of the Er^{3+} ion in the studied glasses, depicting the UV and NIR excitations, and visible and NIR emission transitions, including related NR channels.

theoretically only for all samples as we do not have the facility to measure the Gain experimentally in evaluating background losses of glasses.

3.13. *Energy level scheme*

For all S1–S6 samples, Fig. 10 illustrates Er^{3+} ion's partial energy-level scheme upon $\lambda_{exci.} = 363$ nm, $\lambda_{exci.} = 376$ nm, and 980 nm LD excitations, in which all observed visible and NIR emission transitions and associated NR routes indicated effectively. Under 363 nm and 379 nm pumpings, at first, in all glasses, Er^{3+} ions in $^4I_{15/2}$ ground state are excited to respective $^4G_{9/2}$ and $^4G_{11/2}$ levels and then non-radiatively relax to $^2H_{11/2}$ and $^4S_{3/2}$ levels (thermally equilibrium states). From the $^4S_{3/2}$ state, Er^{3+} ions will rapidly depopulate to the $^4I_{15/2}$ state in a radiative manner emitting green light (550 nm). In sample S1, 454 nm blue emission arises when a part of Er^{3+} ions radiatively relax to $^4I_{15/2}$ state from $^4F_{5/2}$ level. Similarly, upon 980 nm LD pumping, Er^{3+} ions in $^4I_{15/2}$ state stimulate initially to $^4I_{11/2}$ level by absorbing photons and then populate on to metastable $^4I_{13/2}$ level through NR (MPR (multiphonon relaxation)) process. Subsequently, the well-populated Er^{3+} ions in the $^4I_{13/2}$ level will relax radiatively to the $^4I_{15/2}$ state (except the $^4I_{15/2}$ state, there exists no lower energy level close to $^4I_{13/2}$ state), offering NIR fluorescence band peaked at 1.532 μm in all S1–S6 glasses.

As this work is focussed mainly on spectroscopic and luminescence features analysis of all S1–S6 glasses, for all these samples, as a separate work, we are planning to report FTIR, Raman, NMR, XPS, and TGA (Thermogravimetric Analysis) & DSC (Differential Scanning Calorimetry) investigations. Also, to prove that these glasses are suitable for fiber fabrication, glass fibers will be drawn and presented in that work.

4. Conclusions

Optical and luminescence aspects of six Er^{3+}-doped (1 mol%) Li_2O (S1), Na_2O (S2), K_2O (S3), Li_2O–Na_2O (S4), Na_2O–K_2O (S5), and Li_2O–K_2O (S6) separately constituting B_2O_3-rich glasses were analyzed. Absorption spectra showed distinct extended Er^{3+} ion's bands from UV to NIR region. E_{opt} reduced from S1 to S3 sample and S4 to S6 glass specifying higher NBOs creation over BOs in the glass structure. ΔE increased at 0.406–0.440 eV and 0.421–0.442 eV ranges similarly to λ_{edge} trend for S1–S3 and S4–S6 samples and improving ΔE hints at enhanced disorderness in samples with changing alkali (single or mixed) content. Utilizing J-O theory, $\Omega_2>\Omega_6>\Omega_4$ course for S1, S3, S4, S5, and S6 glasses, and $\Omega_2>\Omega_4>\Omega_6$ trend for sample S2 respectively were deduced, and Ω_2 slightly increased from S1 to S3 glass while it reduces for mixed alkali ions in the order S4>S5>S6. Obtained highest Ω_2 for glass S3 reveals a lesser symmetry at Erbium ion sites vicinity and large Er–O bonds' covalency when K_2O added. Under both $\lambda_{exci.} = 363$ nm and $\lambda_{exci.} = 376$ nm, visible luminescence band peaked at 0.55 μm owing to transition Er^{3+}: $^4S_{3/2} \rightarrow {}^4I_{15/2}$ along with a broad luminescence band at 400–500 nm span related to host defects were identified. All S1–S6 samples emit an overall color of purplish-blue to blue and blue to greenish-blue to green upon 363 nm and 376 nm excitations accordingly and derived CP (%) value is the highest for sample S5 under such excitations *i.e.*, 80.7 and 65.2 for purplish-blue and blue emissions. All studied glasses showed $\beta_R = 100\%$ for $^4I_{13/2} \rightarrow {}^4I_{15/2}$ transition, and a broad NIR luminescence band peaked at 1.532 μm ($^4I_{13/2} \rightarrow {}^4I_{15/2}$) was acquired by 980 nm LD excitation. Observed changes in $\Delta\lambda_{eff}$ (S1–S3, 74.66–59.816 nm range and S4–S6, 72.503–64.208 nm span) and σ^{em}_{max} (S1–S6, 6.584–7.249 × 10^{-21} cm^2 range) of $^4I_{13/2} \rightarrow {}^4I_{15/2}$ transition shows the varied alkali ions' influence on Erbium ions' locality in studied samples' network. High σ_{abs} (= 1.459 × 10^{-20} cm^2) of $^4I_{15/2} \rightarrow {}^4I_{13/2}$ transition and large $\Delta\lambda_{eff}$ (= 74.66 nm), better A_R (= 206 s^{-1}), large σ^M_{emi} (= 1.692 × 10^{-20} cm^2), high $\sigma^{em}_{max} \times \Delta\lambda_{eff}$ (= 5.384 × 10^{-26} cm^3), moderate τ_{meas} (= 3.60 ms), including large $G(\lambda, P)$ (= 4.771 dB/cm at $P = 60\%$) of $^4I_{13/2} \rightarrow {}^4I_{15/2}$ transition in sample S1 indicates its competence as an active medium for C-optical band amplification in WDM systems. Also, for $^4I_{13/2} \rightarrow {}^4I_{15/2}$ transition, $\Delta\lambda_{eff}$ and $\sigma^{emi}_{max} \times \Delta\lambda_{eff}$ values in sample S1 are better than those of fluoride (Er^{3+}: ZBLAN) glass respective values. Calculated gain cross-section varied at 1.459–1.692 × 10^{-20} cm^2 range at 1.532 μm for all S1–S6 glasses and attained gain spectra are identified to be positive from $P = 50\%$ and show a flat gain.

CRediT author statement

G. Lakshminarayana: Conceptualization, Methodology, Visualization, Writing - Original Draft, Writing - review & editing, Supervision **A.N. Meza-Rocha**: Investigation, Data Curation, Validation **O. Soriano-Romero**: Investigation **U. Caldiño**: Investigation, Data Curation, Validation **A. Lira**: Formal analysis, Data Curation **Dong-Eun Lee**: Resources, Project administration, Funding acquisition, Supervision **Jonghun Yoon**: Resources, Supervision **Taejoon Park**: Resources, Funding acquisition, Supervision.

Declaration of Competing Interest

The authors declare that they have no known competing financial interests or personal relationships that could have appeared to influence the work reported in this paper.

Acknowledgements

This work was supported by the National Research Foundation of Korea (NRF) grant funded by the Korea government (MSIT) (No. NRF-2018R1A5A1025137).

Appendix A. Supplementary data

Supplementary data to this article can be found online at https://doi.org/10.1016/j.jmrt.2022.04.012.

REFERENCES

[1] Pust P, Weiler V, Hecht C, Tücks A, Wochnik AS, Henβ AK, et al. Narrow-band red-emitting $Sr[LiAl_3N_4]:Eu^{2+}$ as a next-generation LED-phosphor material. Nat Mater 2014;13:891–6.
[2] Erol E, Vahedigharehchopogh N, Kıbrıslı O, Ersundu MÇ, Ersundu AE. Recent progress in lanthanide-doped luminescent glasses for solid-state lighting applications–a review. J Phys: Condens Matter 2021;33:483001. /1–32.
[3] Jha A, Richards B, Jose G, Teddy-Fernandez T, Joshi P, Jiang X, et al. Rare-earth ion doped TeO_2 and GeO_2 glasses as laser materials. Prog Mater Sci 2012;57:1426–91.
[4] Seddon AB, Tang Z, Furniss D, Sujecki S, Benson TM. Progress in rare-earth-doped mid-infrared fiber lasers. Opt Express 2010;18:26704–19.
[5] Cornacchia F, Toncelli A, Tonelli M. 2-μm lasers with fluoride crystals: research and development. Prog Quant Electron 2009;33:61–109.
[6] Basiev TT, Konyushkin VA, Konyushkin DV, Doroshenko ME, Huber G, Reichert F, et al. First visible 639 nm $SrF_2:Pr^{3+}$ ceramic laser. In: *CLEO/Europe and EQEC 2011 conference digest*, OSA technical digest (CD). Optical Society of America; 2011. paper CA2_2.
[7] Tanabe S. Rare-earth-doped glasses for fiber amplifiers in broadband telecommunication. Compt Rendus Chem 2002;5:815–24.
[8] Shen X, Zhu Y, Zhou Y, Li J. Broadband and flat near-infrared emission from Er^{3+}/Tm^{3+} codoped tellurite glass for amplifier applications. J Opt Soc Am B 2020;37:320–8.
[9] Lakshminarayana G, Meza-Rocha AN, Soriano-Romero O, Huerta EF, Caldiño U, Lira A, et al. Pr^{3+}-doped B_2O_3–Bi_2O_3–ZnO–NaF glasses comprising alkali/mixed alkali oxides for potential warm white light generation, blue laser, and E-+S-+C-optical bands amplification applications. J Mater Res Technol 2021;13:2501–26.
[10] Ajithkumar G, Yoo B, Goral DE, Hornsby PJ, Lin A-L, Ladiwala U, et al. Multimodal bioimaging using a rare earth doped Gd_2O_2S:Yb/Er phosphor with upconversion luminescence and magnetic resonance properties. J Mater Chem B 2013;1:1561–72.
[11] Morgan CG, Mitchell AC. Prospects for applications of lanthanide-based upconverting surfaces to bioassay and detection. Biosen Bioelectron 2007;22:1769–75.

[12] Richards BS. Luminescent layers for enhanced silicon solar cell performance: down-conversion. Sol Energy Mater Sol Cells 2006;90:1189–207.
[13] Florêncio L de A, Gómez-Malagón LA, Lima BC, Gomes ASL, Garcia JAM, Kassab LRP. Efficiency enhancement in solar cells using photon down-conversion in Tb/Yb-doped tellurite glass. Sol Energy Mater Sol Cells 2016;157:468–75.
[14] Tu L, Tang G, Qian Q, Yang Z. Controllable structural tailoring for enhanced ~2 μm emission in heavily Tm^{3+}-doped germanate glasses. Opt Lett 2021;46:310–3.
[15] Xia L, Zhang Y, Shen X, Zhou Y. Broad and flat dual-band NIR luminescence from Er^{3+}/Tm^{3+}/Ho^{3+} tri-doped tellurite glass. Opt Lett 2021;46:853–5.
[16] Xu C, Zheng C, Li J, Liu Y, Sun L. ZnS enhancing the infrared emission of Er^{3+} doped oxyfluorosulfide glasses with low hydroxyl content. J Non-Cryst Solids 2021;566:120906.
[17] Sakamoto T, Shimizu M, Yamada M, Kanamori T, Ohishi Y, Terunuma Y, et al. 35-dB gain Tm-doped ZBLYAN fiber amplifier operating at 1.65 μm. IEEE Photon Technol Lett 1996;8:349–51.
[18] Wan R, Wang P, Li S, Ma Y, Zhang G. Spectroscopic properties of ErF_3 doped tellurite–gallium oxyfluoride glass for ~3 μm laser materials. J Appl Phys 2021;129:153105. /1–11.
[19] Yang A, Qiu J, Zhang M, Sun M, Yang Z. Mid-infrared luminescence of Dy^{3+}-doped Ga_2S_3–Sb_2S_3–CsI chalcohalide glasses. Chin Phys B 2018;27:77105. /1–5.
[20] Cui J, Xiao X, Xu Y, Cui X, Chen M, Guo J, et al. Mid-infrared emissions of Dy^{3+} doped Ga-As-S chalcogenide glasses and fibers and their potential for a 4.2 μm fiber laser. Opt Mater Express 2018;8:2089–102.
[21] He H, Jia Z, Wang T, Ohishi Y, Qin W, Qin G. Intense emission at ~3.3 μm from Er^{3+}-doped fluoroindate glass fiber. Opt Lett 2021;46:1057–60.
[22] Mears RJ, Reekie L, Jauncey IM, Payne DN. Low-noise erbium-doped fibre amplifier operating at 1.54 μm. Electron Lett 1987;23:1026–8.
[23] Desurvire E, Simpson JR, Becker PC. High-gain erbium-doped travelling-wave fibre amplifier. Opt Lett 1987;12:888–90.
[24] Miniscalco WJ, Andrews LJ, Zemon S, Hall BT, Wei T, Folweiler RC. Glasses for Er^{3+}-doped fiber lasers and optical amplifiers. MRS Online Proc Libr 1989;172:329–34.
[25] Becker PC, Olsson NA, Simpson JR. Chapter 5 - erbium-doped fiber amplifiers–amplifier basics. In: Becker PC, Olsson NA, Simpson JR, editors. Optics and photonics, erbium-doped fiber amplifiers. Academic Press; 1999. p. 131–52.
[26] Miniscalco WJ. Erbium-doped glasses for fiber amplifiers at 1500 nm. IEEE J. Lightwave Technol. 1991;9:234–50.
[27] Bollond P. OPTICAL AMPLIFIERS | erbrium doped fiber amplifiers for lightwave systems. In: Guenther RD, editor. Encyclopedia of modern optics. Elsevier; 2005, ISBN 9780123693952. p. 275–85.
[28] Jackson SD. Towards high-power mid-infrared emission from a fibre laser. Nat Photonics 2012;6:423–31.
[29] Huang J, Zhang L, Xia L, Shen X, Wei W, You W. Highly efficient ~3.4 μm emission of Er^{3+}-doped TeO_2 based glasses via resonant energy transfer and multi-phonon relaxation processes. Opt Mater 2020;108:110387.
[30] Dorofeev VV, Koltashev VV, Motorin SE, Plekhovich AD, Kim AV. Thermal, optical, and IR-emission properties of extremely low hydroxyl TeO_2-WO_3-Bi_2O_3-La_2O_3-xEr_2O_3 glasses for mid-infrared photonics. Photonics 2021;8:320–321–13.
[31] Cai M, Wei T, Zhou B, Tian Y, Zhou J, Xu S, et al. Analysis of energy transfer process based emission spectra of erbium doped germanate glasses for mid-infrared laser materials. J Alloys Compd 2015;626:165–72.
[32] El-Maaref AA, Wahab EAA, Shaaban Kh S, El-Agmy RM. Enhancement of spectroscopic parameters of Er^{3+}-doped cadmium lithium gadolinium silicate glasses as an active medium for lasers and optical amplifiers in the NIR-region. Solid State Sci 2021;113:106539.
[33] Caetano M, Silva ACA, Filho JCS, de Morais RF, Sales TO, Andrade AA, et al. High quantum efficiency of Er^{3+} ions in phosphate glasses: controlled atmosphere and addition of fluoride. J Lumin 2020;228:117599.
[34] Deopa N, Sahu MK, Kaur S, Prasad A, Swapna K, Kumar V, et al. Enhanced visible green and 1.5 μm radiative emission of Er^{3+} ions in Li_2O-PbO-Al_2O_3-B_2O_3 glasses for photonic applications. J Rare Earths 2021;39:520–5.
[35] Madhu A, Srinatha N. Structural and spectroscopic studies on the concentration dependent erbium doped lithium bismuth boro tellurite glasses for optical fiber applications. Infrared Phys Technol 2020;107:103300.
[36] Zhang W, Lin L, Lan B, Liu J, Chen Y, Zhou G, et al. Er^{3+}-doped antimony-silica glass and fiber for broadband optical amplification. J Am Ceram Soc 2021;104:5584–92.
[37] Zhang FF, Zhang WJ, Yuan J, Chen DD, Qian Q, Zhang QY. Enhanced 2.7 μm emission from Er^{3+} doped oxyfluoride tellurite glasses for a diode-pump mid-infrared laser. AIP Adv 2014;4:47101. /1–11.
[38] Zhang J, Wang R, Wang X, Li W, Liu M, Jia S, et al. Efficient 3.5 μm mid-infrared emission in heavily Er^{3+}-doped fluoroaluminate glasses and its emission mechanism. J Lumin 2021;238:118301.
[39] Yang Z, Pan H, Chen Y, Wang R, Shen X. Emission properties of Er^{3+}-doped $Ge_{20}Ga_5Sb_{10}Se_{65}$ glasses in near- and mid-infrared. Infrared Phys Technol 2018;89:277–81.
[40] Zhang J -j, Zhang X -s, Li L, Wu S -h, Yin H, Liu X, et al. Enhanced mid-infrared emission of non-oxide erbium doped fluorochloride glass. Optoelectron Lett 2020;16:360–4.
[41] Bengisu M. Borate glasses for scientific and industrial applications: a review. J Mater Sci 2016;51:2199–242.
[42] Eigen M. Chapter 12 - OXIDE GLASSES. In: Rao KJ, editor. Structural chemistry of glasses. Elsevier Science Ltd; 2002, ISBN 9780080439587. p. 463–511.
[43] Konijnendijk WL, Stevels JM. The structure of borate glasses studied by Raman scattering. J Non-Cryst Solids 1975;18:307–31.
[44] Lakshminarayana G, Meza-Rocha AN, Soriano-Romero O, Huerta EF, Caldiño U, Lira A, et al. Analysis of fluorescence characteristics of Sm^{3+}-doped B_2O_3-rich glasses for Orange-light-emitting diodes. J Alloys Compd 2021;884:161076.
[45] Pan HB, Zhao XL, Zhang X, Zhang KB, Li LC, Li ZY, et al. Strontium borate glass: potential biomaterial for bone regeneration. J R Soc Interface 2010;7:1025–31.
[46] Arya SK, Danewalia SS, Singh K. Frequency independent low-*k* lithium borate nanocrystalline glass ceramic and glasses for microelectronic applications. J Mater Chem C 2016;4:3328–36.
[47] Bhattacharya S, Ghosh A. Relaxation of silver ions in superionic borate glasses. Chem Phys Lett 2006;424:295–9.
[48] Santos SNC, Almeida JMP, Paula KT, Tomazio NB, Mastelaro VR, Mendonça CR. Characterization of the third-order optical nonlinearity spectrum of barium borate glasses. Opt Mater 2017;73:16–9.
[49] Erenturk SA, Bengisu M, Erdogan C. Evaluation of sodium borate glasses for radioactive waste immobilization applications. J Radioanal Nucl Chem 2017;314:2069–86.
[50] ALMisned G, Tekin HO, Kavaz E, Bilal G, Issa SAM, Zakaly HMH, et al. Gamma, fast neutron, proton, and alpha shielding properties of borate glasses: a closer look on lead (II) oxide and bismuth (III) oxide reinforcement. Appl Sci 2021;11:6837. 1–20.
[51] Bhattacharya S, Shashikala HD. Effect of BaO on thermal and mechanical properties of alkaline earth borosilicate glasses with and without Al_2O_3. Phys B: Condens Matter 2019;571:76–86.

[52] Yu H, Chen Q, Jin Zh. Thermodynamic reassessment of the $BaO-B_2O_3$ system. J Phase Equil 1999;20:479–84.
[53] Colak SC, Akyuz I, Atay F. On the dual role of ZnO in zinc-borate glasses. J Non-Cryst Solids 2016;432:406–12.
[54] Lakshminarayana G, Meza-Rocha AN, Soriano-Romero O, Huerta EF, Caldiño U, Lira A, et al. Survey of optical and fluorescence traits of Tm^{3+}-doped alkali/mixed alkali oxides constituting B_2O_3-BaO-ZnO-LiF glasses for 0.45 μm laser and 1.46 μm fiber amplifier. Results Phys 2021;26:104343.
[55] Kim D-N, Lee J -y, Huh J-S, Kim H -s. Thermal and electrical properties of $BaO–B_2O_3–ZnO$ glasses. J Non-Cryst Solids 2002;306:70–5.
[56] Zhong J, Bray PJ. Change in boron coordination in alkali borate glasses, and mixed alkali effects, as elucidated by NMR. J Non-Cryst Solids 1989;111:67–76.
[57] Judd BR. Optical absorption intensities of rare-earth ions. Phys Rev. 1962;127:750–61.
[58] Ofelt GS. Intensities of crystal spectra of rare-earth ions. J Chem Phys 1962;37:511–20.
[59] Luo M, Chen B, Li X, Zhang J, Xu S, Zhang X, et al. Fluorescence decay route of optical transition calculation for trivalent rare earth ions and its application for Er^{3+}-doped $NaYF_4$ phosphor. Phys Chem Chem Phys 2020;22:25177–83.
[60] Zhang Y, Chen B, Xu S, Li X, Zhang J, Sun J, et al. A universal approach for calculating the Judd–Ofelt parameters of RE^{3+} in powdered phosphors and its application for the β-$NaYF_4$:Er^{3+}/Yb^{3+} phosphor derived from auto-combustion-assisted fluoridation. Phys Chem Chem Phys 2018;20:15876–83.
[61] Luo W, Liao J, Li R, Chen X. Determination of Judd–Ofelt intensity parameters from the excitation spectra for rare-earth doped luminescent materials. Phys Chem Chem Phys 2010;12:3276–82.
[62] Sayyed MI, Lakshminarayana G, Moghaddasi M, Kityk IV, Mahdi MA. Physical properties, optical band gaps and radiation shielding parameters exploration for Dy^{3+}-doped alkali/mixed alkali multicomponent borate glasses. Glass Phys Chem 2018;44:279–91.
[63] Duffy JA. A common optical basicity scale for oxide and fluoride glasses. J Non-Cryst Solids 1989;109:35–9.
[64] Danilyuk PS, Popovich KP, Puga PP, Gomonai AI, Primak NV, Krasilinets VN, et al. Optical absorption spectra and energy levels of Er^{3+} ions in glassy lithium tetraborate matrix. Opt Spectrosc 2014;117:759–63.
[65] Mariselvam K, Liu J. A novel Er^{3+} ions doped zirconium magnesium borate glass with very high quantum efficiency for green laser and optical amplifier applications. Solid State Sci 2021;111:106443.
[66] Rajagukguk J, Fitrilawati, Sinaga B, Kaewkhao J. Structural and spectroscopic properties of Er^{3+} doped sodium lithium borate glasses. Spectrochim Acta A Mol Biomol Spectrosc 2019;223:117342.
[67] Taherunnisa Sk, Reddy DVK, Rao TS, Rudramamba KS, Zhydachevskyy YA, Suchocki A, et al. Effect of up-conversion luminescence in Er^{3+} doped phosphate glasses for developing Erbium-Doped Fibre Amplifiers (EDFA) and G-LED's. Opt Mater X 2019;3:100034.
[68] Abdel-Baki M, Abdel-Wahab FA, El-Diasty F. One-photon band gap engineering of borate glass doped with ZnO for photonics applications. J Appl Phys 2012;111:73506. /1–10.
[69] Mizrahi V, DeLong KW, Stegeman GI, Saifi MA, Andrejco MJ. Two-photon absorption as a limitation to all-optical switching. Opt Lett 1989;14:1140–2.
[70] Kaminskii AA. Crystalline lasers: physical processes and operating schemes (laser & optical science & technology series). Boca Raton, U.S.A: CRC Press; 1996. pp 274.
[71] Bolton J. New NIR emission from Sm^{3+} in Yb^{3+}-Sm^{3+} co-doped tellurite glass. J Lumin 2021;231:117717.
[72] Lakshminarayana G, Baki SO, Lira A, Kityk IV, Caldiño U, Kaky KM, et al. Structural, thermal and optical investigations of Dy^{3+}-doped $B_2O_3–WO_3–ZnO–Li_2O–Na_2O$ glasses for warm white light emitting applications. J Lumin 2017;186:283–300.
[73] Tanabe S, Ohyagi T, Soga N, Hanada T. Compositional dependence of Judd-Ofelt parameters of Er^{3+} ions in alkali-metal borate glasses. Phys Rev B 1992;46:3305–10.
[74] Jiang S, Luo T, Hwang B-C, Smekatala F, Seneschal K, Lucas J, et al. Er^{3+}-doped phosphate glasses for fiber amplifiers with high gain per unit length. J Non-Cryst Solids 2000;263–264:364–8.
[75] Rodríguez-Mendoza UR, Lalla EA, Cáceres JM, Rivera-López F, León-Luís SF, Lavín V. Optical characterization, 1.5 μm emission and IR-to-visible energy upconversion in Er^{3+}-doped fluorotellurite glasses. J Lumin 2011;131:1239–48.
[76] Devarajulu G, Ravi O, Reddy CM, Ahamed Sd ZA, Raju BDP. Spectroscopic properties and upconversion studies of Er^{3+}-doped SiO_2-Al_2O_3-Na_2CO_3-SrF_2-CaF_2 oxyfluoride glasses for optical amplifier applications. J Lumin 2018;194:499–506.
[77] Aull BF, Jenssen HP. Vibronic interactions in Nd:YAG resulting in nonreciprocity of absorption and stimulated emission cross sections. IEEE J Quant Electron 1982;18:925–30.
[78] Jha A, Shen S, Naftaly M. Structural origin of spectral broadening of 1.5-μm emission in Er^{3+}-doped tellurite glasses. Phys Rev B 2000;62:6215–27.
[79] Shi DM, Zhao YG, Wang XF, Liao GH, Zhao C, Peng MY, et al. Effects of alkali ions on thermal stability and spectroscopic properties of Er^{3+}-doped gallogermanate glasses. Phys B 2011;406:628–32.
[80] Lei W, Chen B, Zhang X, Pun EYB, Lin H. Optical evaluation on Nd^{3+}-doped phosphate glasses for O-band amplification. Appl Opt 2011;50:835–41.
[81] Klinkov VA, Tsimerman EA, Rokhmin AS, Andreeva VD, Tagil'tseva NO, Babkina A, et al. 1.53 μm luminescent properties of Er^{3+}-doped fluoroaluminate glasses. 2021 Opt Mater 2021;121:111585.
[82] McCumber DE. Einstein relations connecting broadband emission and absorption spectra. Phys Rev. 1964;136:A954–7.
[83] Mariyappan M, Arunkumar S, Marimuthu K. Judd-Ofelt analysis and NIR luminescence investigations on Er^{3+} ions doped $B_2O_3–Bi_2O_3–Li_2O–K_2O$ glasses for photonic applications. Phys B 2019;572:27–35.